

# THE MOSDEF SURVEY: MEASUREMENTS OF BALMER DECREMENTS AND THE DUST ATTENUATION CURVE AT REDSHIFTS $z \sim 1.4\text{--}2.6^*$

NAVEEN A. REDDY<sup>1,5</sup>, MARISKA KRIEK<sup>2</sup>, ALICE E. SHAPLEY<sup>3</sup>, WILLIAM R. FREEMAN<sup>1</sup>, BRIAN SIANA<sup>1</sup>, ALISON L. COIL<sup>4</sup>,  
BAHRAM MOBASHER<sup>1</sup>, SEDONA H. PRICE<sup>2</sup>, RYAN L. SANDERS<sup>3</sup>, AND IRENE SHIVAEI<sup>1</sup>

<sup>1</sup> Department of Physics and Astronomy, University of California, Riverside, 900 University Avenue, Riverside, CA 92521, USA

<sup>2</sup> Astronomy Department, University of California, Berkeley, CA 94720, USA

<sup>3</sup> Department of Physics & Astronomy, University of California, Los Angeles, 430 Portola Plaza, Los Angeles, CA 90095, USA

<sup>4</sup> Center for Astrophysics and Space Sciences, University of California, San Diego, 9500 Gilman Dr., La Jolla, CA 92093-0424, USA

Received 2015 February 4; accepted 2015 April 9; published 2015 June 23

## ABSTRACT

We present results on the dust attenuation curve of  $z \sim 2$  galaxies using early observations from the MOSFIRE Deep Evolution Field survey. Our sample consists of 224 star-forming galaxies with  $z_{\text{spec}} = 1.36\text{--}2.59$  and high signal-to-noise ratio measurements of  $H\alpha$  and  $H\beta$  obtained with Keck/MOSFIRE. We construct composite spectral energy distributions (SEDs) of galaxies in bins of Balmer decrement to measure the attenuation curve. We find a curve that is similar to the SMC extinction curve at  $\lambda \gtrsim 2500 \text{ \AA}$ . At shorter wavelengths, the shape is identical to that of the Calzetti et al. relation, but with a lower normalization. Hence, the new attenuation curve results in star formation rates (SFRs) that are  $\approx 20\%$  lower, and stellar masses that are  $\Delta \log(M^*/M_\odot) \simeq 0.16$  dex lower, than those obtained with the Calzetti relation. We find that the difference in the total attenuation of the ionized gas and stellar continuum correlates strongly with SFR, such that for dust-corrected SFRs  $\gtrsim 20 M_\odot \text{ yr}^{-1}$ , assuming a Chabrier initial mass function, the nebular emission lines suffer an increasing degree of obscuration relative to the continuum. A simple model that can account for these trends is one in which the UV through optical stellar continuum is dominated by a population of less-reddened stars, while the nebular line and bolometric luminosities become increasingly dominated by dustier stellar populations for galaxies with large SFRs, as a result of the increased dust enrichment that accompanies such galaxies. Consequently, UV- and SED-based SFRs may underestimate the total SFR at even modest levels of  $\approx 20 M_\odot \text{ yr}^{-1}$ .

*Key words:* dust, extinction – galaxies: evolution – galaxies: formation – galaxies: high-redshift – galaxies: star formation

## 1. INTRODUCTION

As a fundamental byproduct of star formation, dust plays an important role in our understanding of heavy element synthesis in stars, the dispersal of such elements into the ISM, and our interpretation of the stellar populations of galaxies given the wavelength-dependent effects of dust absorption. The latter aspect is encoded in the shape of the attenuation curve (Draine & Li 2007), which conveniently parameterizes the complexities of the dust properties and spatial distribution of that dust with respect to the stars in galaxies. Observations of the Milky Way and nearby galaxies have yielded detailed information on the shape of the dust extinction and attenuation curves, respectively, in the local universe (e.g., Prevot et al. 1984; Cardelli et al. 1989; Pei 1992; Calzetti et al. 1994, 2000; Gordon et al. 2003; Johnson et al. 2007a; Wild et al. 2011). Armed with such information, one can then deduce the amount of attenuation at any given wavelength (i.e., the dust obscuration) and recover the bolometric star formation rate (SFR), accounting for the starlight absorbed and re-radiated by dust.

Understanding the shape of this curve takes on added importance for evaluating the global energetics and stellar populations of galaxies at high redshift, where direct measures of dust emission from far-infrared (far-IR) data become

observationally inaccessible for typical star-forming galaxies (e.g., Reddy et al. 2006). The stacking of mid- and far-IR data from the *Spitzer Space Telescope* and the *Herschel Space Observatory* has proved beneficial for our understanding of the average dust properties of typical  $L^*$  star-forming galaxies at  $z \sim 2$  (Reddy et al. 2006; Daddi et al. 2007; Reddy et al. 2012a). IR observations of lensed star-forming galaxies can lend insight into the dust emission from individual  $L^*$  (and fainter) galaxies (e.g., Siana et al. 2008, 2009; Sklias et al. 2014), but these samples remain small. These stacking and lensed galaxy studies lack the precision required to uncover changes in dust properties and dust/stars geometry from galaxy to galaxy. Further, while the UV continuum slope (e.g., Calzetti et al. 1994; Meurer et al. 1999) has been shown by numerous studies to be a reasonable proxy for dust attenuation in star-forming galaxies in the local and high-redshift Universe (e.g., Calzetti et al. 1994; Meurer et al. 1999; Adelberger & Steidel 2000; Nandra et al. 2002; Reddy et al. 2006, 2010, 2012a; Daddi et al. 2007; Overzier et al. 2011; Buat et al. 2012, among many others), and while it can be measured for individual galaxies to very faint magnitudes at high redshift (Bouwens et al. 2012; Dunlop et al. 2012; Finkelstein et al. 2012; Oesch et al. 2013), it is nonetheless also sensitive to age, metallicity, and star formation history (e.g., Kong et al. 2004; Seibert et al. 2005; Johnson et al. 2007b; Dale et al. 2009; Reddy et al. 2010; Boquien et al. 2012; Wilkins et al. 2013; see also below). In addition, the measurement of the UV slope can be complicated by the presence of the 2175 Å absorption feature (Noll et al. 2009;

\* Based on data obtained at the W.M. Keck Observatory, which is operated as a scientific partnership among the California Institute of Technology, the University of California, and NASA, and was made possible by the generous financial support of the W.M. Keck Foundation.

<sup>5</sup> Alfred P. Sloan Research Fellow.

Buat et al. 2011, 2012; Kriek & Conroy 2013). Despite these issues, the UV slope is by far the most heavily used dust indicator at high redshift, given that it can be measured easily for individual star-forming galaxies, particularly those selected by their rest-frame UV colors.

Separately, existing studies of the shape of the attenuation curve at  $z \gtrsim 1.5$  have relied either on spectroscopy over limited wavelength ranges, indirect inferences based on spectral energy distribution (SED) modeling of broad- and medium-band data and/or SFR comparisons (Erb et al. 2006a; Noll et al. 2009; Reddy et al. 2006, 2010; Buat et al. 2011, 2012; Kriek & Conroy 2013), or have been investigated for galaxies over a limited range of spectral shape (e.g., galaxies with weak Balmer and 4000 Å breaks) and UV luminosities with an explicit assumption for the shape of the intrinsic spectrum (Scoville et al. 2015). What have been needed for a more robust study of the attenuation curve are indicators of dust and SFR at high redshift that: (a) can be measured for individual  $L^*$  galaxies at high redshift; (b) are less attenuated than the UV luminosity; (c) are less sensitive to age and star formation history; and (d) probe star formation on the shortest timescales. When coupled with samples of galaxies with near-infrared (near-IR) spectra and broad- and intermediate-band photometry spanning the UV through near-IR wavelengths, these SFR/dust indicators can be used to address the shape of the attenuation curve of high-redshift galaxies.

The H I recombination line luminosities and their ratios have been considered the “gold standard” for measuring SFRs and dust attenuation in local galaxies (Kennicutt & Evans 2012). In particular, the Balmer (and higher series) transitions in star-forming galaxies arise from the H II regions generated by the most massive O stars ( $\gtrsim 8 M_\odot$ ) and therefore trace the SFR averaged over timescales of just a few Myr, making these tracers insensitive to the star formation history on longer timescales. In nearby galaxies, these lines are easily observable from the ground to faint limits, and they are less affected by attenuation than UV emission. The higher series lines, including Pa $\alpha$  ( $\lambda = 1.875 \mu\text{m}$ ) and Br $\gamma$  ( $\lambda = 2.166 \mu\text{m}$ ), are particularly useful indicators because their relatively long wavelengths imply negligible dust absorption. However, these features are weak relative to the Balmer lines and, at  $z \gtrsim 1.5$ , shift into the mid-IR where current instrumentation has been insufficient to detect the lines for all but the most luminous and strongly gravitationally lensed galaxies (Papovich et al. 2009).

Until recently, obtaining measurements of nebular recombination (other than Ly $\alpha$ ) has been prohibitive for faint galaxies at redshifts  $z \gtrsim 0.5$  because these lines are shifted into the near-IR where the terrestrial background is substantially higher than in the optical, with a color of  $(B - K_s) \simeq 7$  mag. Deep ground-based narrowband imaging (Geach et al. 2008; Lee et al. 2012; Ly et al. 2012; Sobral et al. 2012; Momcheva et al. 2013), and space-based grism spectroscopy afforded by the *Hubble Space Telescope* (HST) WFC3 camera (Atek et al. 2010; Brammer et al. 2012; Domínguez et al. 2013; Price et al. 2014) have begun to advance the study of nebular line emission (particularly H $\alpha$  and H $\beta$ ) in intermediate-redshift galaxies ( $0.5 \lesssim z \lesssim 2.5$ ). Nonetheless, such studies are generally limited to detecting high equivalent width lines, do not allow for the separation of lines close in wavelength (e.g., H $\alpha$  and [N II]), or have a low resolution ( $R < 130$ ) with a limited wavelength range that hinders the determination of physically

important line ratios and widths. Moderate-resolution near-IR spectroscopy exists for both UV-selected star-forming galaxies (Erb et al. 2006b; Mannucci et al. 2009) and near-IR-selected samples of massive ( $M \gtrsim 10^{11} M_\odot$ ) galaxies (Kriek et al. 2008), yet these samples are quite small and typically do not cover both the H $\alpha$  and H $\beta$  lines. In cases where both lines were targeted (e.g., Kriek et al. 2008), the H $\beta$  line is commonly undetected given the depths of previous spectroscopic campaigns. The advances enabled with the new generation of multi-object near-IR spectrographs on 8–10-m-class telescopes have begun to remedy these past deficiencies in high-redshift near-IR spectroscopy (e.g., Kashino et al. 2013; Steidel et al. 2014).

To this end, we have begun the MOSFIRE Deep Evolution Field (MOSDEF) survey (Kriek et al. 2015), conducted with the recently commissioned multi-object near-IR spectrograph MOSFIRE (McLean et al. 2012) on the Keck I telescope. MOSDEF aims to characterize the SFRs, dust attenuation, chemical content, ISM physical conditions, dynamics, stellar populations, and black hole accretion activity of a large sample of  $\sim 1500$  H-selected galaxies and active galactic nuclei (AGN) in the redshift range  $z = 1.4$ – $3.8$ , corresponding to the peak of star formation (see review of Madau & Dickinson 2014) and AGN activity (e.g., Silverman et al. 2008). In this study, we use a sample of 224 galaxies with measurements of the H $\alpha$  and H $\beta$  emission lines from the first two years of the MOSDEF survey to provide a direct measurement of the shape of the attenuation curve over the full wavelength range from the UV through near-IR for typical star-forming galaxies at  $z \gtrsim 1.4$ . Our analysis marks a significant improvement over existing studies because (a) we consider galaxies with a large range in spectral shapes (from very blue and dust-free star-forming galaxies to very dusty and highly star-forming ones); (b) we use an indicator of dust, namely the Balmer decrement, which is sensitive to the reddening of the ionized gas and thus is physically distinct from the shape of the SED (and thus less sensitive to the details of the star formation history and age of the stellar population), and which can be measured for individual galaxies in our sample; (c) our method of computing the attenuation curve is model-independent, in that we make no assumption of the shape of the intrinsic SED—rather, we use the data themselves to establish the how galaxy spectral shapes vary with increased dust attenuation; and (d) the extensive multi-wavelength photometry affords us the ability to measure the shape of the attenuation curve at long wavelengths and, thus, the normalization of the curve.

In Section 2, we introduce the MOSDEF survey and the basic measurements including line fluxes, stellar population parameters, and SFRs. Section 3 presents a discussion of the effects of dust on the stellar continuum and the derivation of the attenuation curve. The implications for the attenuation curve on our inferences of the stellar populations and SFRs, as well as the total attenuation of the stellar continuum and ionized gas, in distant galaxies are discussed in Section 4. Throughout we assume a Chabrier (2003) initial mass function (IMF) and a cosmology with  $H_0 = 70 \text{ km s}^{-1} \text{ Mpc}^{-1}$ ,  $\Omega_\Lambda = 0.7$ , and  $\Omega_m = 0.3$ . Line wavelengths are in vacuum. All magnitudes are expressed in the AB system (Oke & Gunn 1983).

## 2. DATA AND BASIC MEASUREMENTS

### 2.1. MOSDEF Survey

The MOSDEF survey is being conducted using the MOSFIRE spectrograph (McLean et al. 2012; Steidel et al. 2014) on the 10 m Keck I telescope. This recently commissioned instrument enables the simultaneous near-IR spectroscopy of up to  $\approx 46$  (with typically 30) galaxies across a  $6' \times 3'$  field of view. MOSFIRE provides a wavelength coverage from 0.97 to  $2.40 \mu\text{m}$  with a spectral resolution of  $R \approx 3300, 3650,$  and  $3600$  in the  $J, H,$  and  $K$  bands, respectively. Details of the survey, observations, and data reduction are provided in Kriek et al. (2014), and below we summarize the salient aspects relevant for this analysis, which uses the current data from the first two observing seasons of the survey.

### 2.2. Galaxy Selection

Catalogs including ground- and space-based photometry from 0.3 to  $8.0 \mu\text{m}$ , which were provided to us by the 3D-*HST* grism survey team (PI: van Dokkum; Brammer et al. 2012; Skelton et al. 2014), were used for target selection (Kriek et al. 2015). These catalogs are based on sources detected in a weighted combination of the *HST* F125W, F140W, and F160W images in the five fields of the Cosmic Assembly Near-Infrared Deep Extragalactic Legacy Survey (Koekemoer et al. 2011; Grogin et al. 2011): COSMOS, EGS, GOODS-North, GOODS-South, and UDS. The *targeting* catalogs include photometric redshifts and, where available, *HST* grism redshifts (Brammer et al. 2012; Skelton et al. 2014) and external spectroscopic redshifts. We restricted the targeting catalogs to include only those galaxies with photometric and/or grism or external spectroscopic redshifts in the three ranges  $z = 1.37\text{--}1.70, 2.09\text{--}2.61,$  and  $2.95\text{--}3.80$ , where the various strong nebular emission lines of interest, including  $[\text{O II}] \lambda\lambda 3727, 3730 \text{ \AA}, [\text{O III}] \lambda\lambda 4364, 5008 \text{ \AA}, \text{H}\beta, \text{H}\alpha,$  and  $[\text{N II}] \lambda\lambda 6550, 6585 \text{ \AA},$  fall in the  $Y, J, H,$  and  $K$  atmospheric windows. Targets are selected to fixed  $H$ -band magnitude limits of  $m_{\text{F160W}} = 24.0, 24.5,$  and  $25.0$ , for the  $z = 1.37\text{--}1.70, 2.09\text{--}2.61,$  and  $2.95\text{--}3.80$  redshift ranges, respectively, to ensure a roughly consistent stellar mass limit of  $\approx 10^9 M_{\odot}$  across the three redshift ranges. For brevity, we refer to these as the  $z \sim 1.5, 2.3,$  and  $3.3$  samples. In this analysis, we consider only galaxies from the two lower redshift ranges, where both the  $\text{H}\alpha$  and  $\text{H}\beta$  lines are covered.

### 2.3. Observations and Efficiency

Targets were prioritized for spectroscopic observations based on two primary criteria. First, bright galaxies were up-weighted relative to fainter galaxies to ensure a statistical representation of rarer, massive galaxies. Second, within a given magnitude range, objects were prioritized according to whether they had external spectroscopic redshifts, grism redshifts, photometric redshifts toward the center of the redshift ranges specified above, and photometric redshifts at the edges of the redshift ranges, in that order. The sample characteristics, success rate, and comparison of the spectroscopic sample to the parent sample are presented in Kriek et al. (2015). Masks were observed using an ABA'B' dither pattern with  $0''.7$  width slits for 2 hr each in the  $J, H,$  and  $K$  filters for the  $z \sim 2.3$  sample; and 1 hr each in the  $Y, J,$  and  $H$  filters for the  $z \sim 1.5$  sample. Our observations were taken with a typical seeing of  $0''.4\text{--}1''.0$ .

Data reduction and spectral extraction were accomplished using a custom IDL pipeline and interactive software (Kriek et al. 2015). The prioritization and exposure time strategy have proved highly successful, with an  $\sim 80\%$  spectroscopic confirmation rate on average per mask, and a  $\gtrsim 70\%$  success rate for objects at the faint limit of our  $z \sim 2.3$  sample. Figure 1 shows the spectroscopic redshift distribution of 259 galaxies (excluding X-ray and IR-selected AGN; Coil et al. 2015) in the two lower redshift ranges targeted with MOSDEF thus far.

### 2.4. Slit Loss Corrections

Slit loss corrections have a particular bearing on our analysis because they are required to ensure accurate flux ratios between lines taken through different photometric filters and observed under different weather conditions. Response corrections of the spectra were performed using telluric standard star observations, and an initial flux calibration is implemented by forcing the spectra of a bright ‘‘slit star’’ placed on each of the science masks to match the star’s broadband photometry. However, the typical seeing of our observations is such that most of the targeted galaxies are spatially resolved and thus cannot be treated as point sources when correcting for the loss of flux outside the slit apertures. Thus, we modeled the F160W light profiles of each of our galaxies using a two-dimensional rotated elliptical Gaussian, which, when convolved with the seeing disk and integrated through the slit, yields an estimate of the fraction of flux lost outside the slit, relative to the fraction lost for the slit star. The efficacy of this procedure is evaluated by comparing the spectroscopic magnitudes of galaxies detected in the continuum with their broadband magnitudes. Our slit loss correction procedure yields an absolute spectral flux calibration that is typically within 18% of that predicted from the photometry, with a dispersion of roughly the same order.

### 2.5. Line Flux Measurements

Line measurements were performed by first estimating an initial redshift based on the highest signal-to-noise ratio (S/N) line for each galaxy, and then fitting Gaussian functions at the observed wavelengths of all other lines. We allowed for a linear fit to the continuum underlying each line, and the  $[\text{O II}] \lambda 3727, 3730$  and  $\text{H}\alpha + [\text{N II}] \lambda 6550, 6585$  lines were fit using double and triple Gaussian functions, respectively. To estimate line flux errors, the spectra of each galaxy were perturbed 1000 times according to their error spectra, and all the lines were remeasured from these realizations.

The  $\text{H}\alpha$  and  $\text{H}\beta$  line fluxes were corrected for underlying Balmer absorption arising primarily from the atmospheres of A stars. As the continuum is generally undetected in the MOSDEF spectra, we estimated the Balmer absorption from the stellar population model fits to the galaxies, as discussed in the next section. For each model fit, we measured the absorbed flux relative to the continuum. Generally, the corrections reach peak rest-frame equivalent widths of  $\lesssim 3$  and  $\lesssim 4 \text{ \AA}$  for  $\text{H}\alpha$  and  $\text{H}\beta$ , respectively, at an age of 500 Myr. For a constant star formation history, the equivalent widths equilibrate to  $\approx 2\text{--}3 \text{ \AA}$  for older ages. The typical corrections to the  $\text{H}\alpha$  and  $\text{H}\beta$  emission line fluxes are  $\lesssim 3\%$  and  $\lesssim 10\%$ , respectively. The corrected  $\text{H}\alpha/\text{H}\beta$  ratios for our sample are shown in Figure 1. The random uncertainties in the Balmer absorption line fluxes were estimated by calculating the dispersion in the absorbed fluxes for model stellar population fits to the photometry

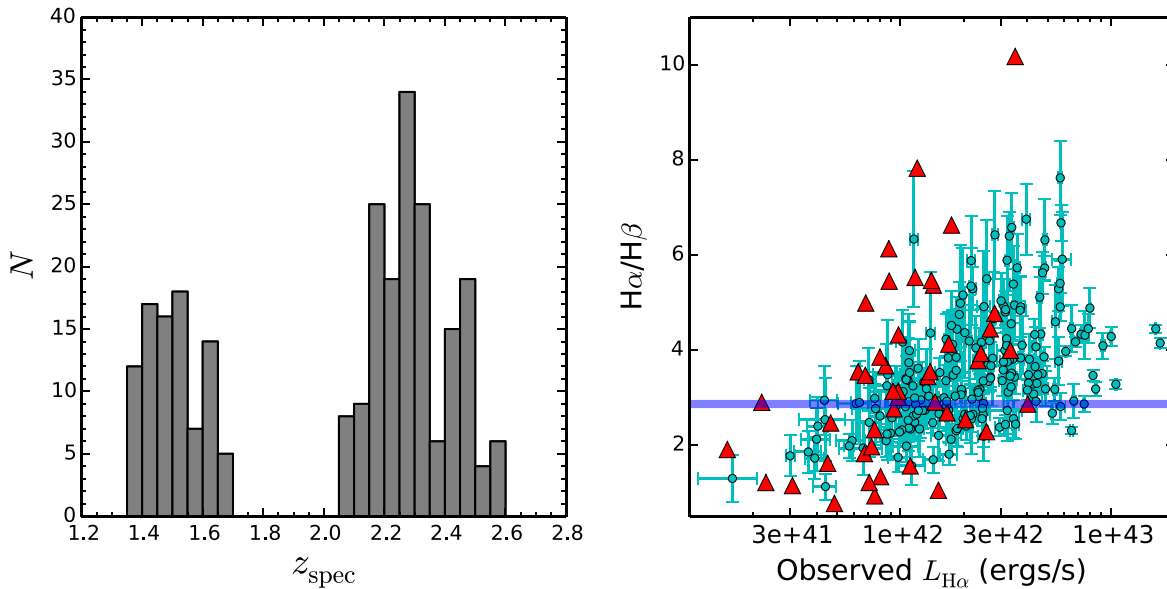


**Figure 1.** Left: spectroscopic redshift distribution of 259 galaxies in the two lower redshift ranges ( $z = 1.37\text{--}1.70$  and  $2.09\text{--}2.61$ ) targeted with MOSDEF during the first two observing seasons. Right: ratio of  $H\alpha$  to  $H\beta$  emission flux vs. observed  $H\alpha$  luminosity, for our sample of 259 galaxies with spectroscopic redshifts  $1.35 < z_{\text{spec}} < 2.59$  and  $S/N_{H\alpha} \geq 3$ . The emission line fluxes are corrected for underlying Balmer absorption. The 46 galaxies with  $3\sigma$  upper limits in  $H\beta$  flux are denoted by the triangles. The horizontal blue line indicates the intrinsic ratio ( $H\alpha/H\beta = 2.86$ ) for typical ISM conditions (Osterbrock 1989). Of the 213 galaxies with significant detections of both  $H\alpha$  and  $H\beta$ , 58 and 85 are consistent with having non-zero nebular attenuation at the  $3\sigma$  and  $2\sigma$  levels, respectively.

perturbed many times according to the photometric errors. The uncertainties in the absorbed fluxes are  $\simeq 2\%$  and much smaller than the typical  $\approx 15\%$  uncertainties in the emission line flux measurements, and therefore we chose not to include the additional random error of the absorbed fluxes in our analysis.

It is useful to assess whether the 46 galaxies with  $3\sigma$  upper limits in  $H\beta$  have distinctive properties relative to those of the 213  $H\beta$ -detected galaxies. The 46  $H\beta$ -undetected galaxies have lower limits in  $H\alpha/H\beta$  that span the full range observed for the  $H\beta$ -detected galaxies, and the broadband SEDs for the former are otherwise unremarkable compared to the latter. Moreover, the frequency with which the  $H\beta$  line is significantly affected by strong skylines is much higher (37 out of 46, or 80%) for the  $H\beta$ -undetected galaxies than for the  $H\beta$ -detected galaxies (60 out of 213, or 28%). Thus, the  $H\beta$  non-detections can at least partly be attributed to the fact that the galaxies lie at redshifts where  $H\beta$  happened to fall on or close to a strong skyline.

To further investigate any systematic differences between these 46 galaxies and the rest of the sample, we constructed weighted average spectra of the  $H\beta$ -detected and  $H\beta$ -undetected galaxies, and measured the  $H\alpha$  and  $H\beta$  fluxes in these combined spectra. The weighting of individual spectra when computing the average is simply  $1/\sigma(\lambda)^2$ , where  $\sigma(\lambda)$  is the value of the error spectrum at wavelength  $\lambda$ . The  $H\beta$ -detected and  $H\beta$ -undetected galaxies have  $\langle H\alpha/H\beta \rangle = 4.1$  and 4.3, respectively, after correcting for the mean Balmer absorption in these galaxies. This difference is smaller than the dispersion in the mean Balmer decrements obtained when we bootstrap resample the galaxies contributing to the mean stacks. The galaxies with undetected  $H\beta$  have an average Balmer decrement that is similar to that of the  $H\beta$ -detected galaxies, implying that they suffer the same degree of obscuration on average. Only those galaxies with  $>3\sigma$  detection of  $H\beta$  (and  $H\alpha$ ) are considered in the derivation of

the attenuation curve, but we specifically include the sample of  $H\beta$ -undetected galaxies throughout the paper as necessary.

## 2.6. Stellar Population Modeling

To aid our analysis, we modeled the stellar populations of galaxies in our sample to derive SED-based SFRs, color excesses, ages, and stellar masses. The basic procedure was to model the multi-wavelength photometry of the galaxies using a suite of Bruzual & Charlot (2003) stellar population models for different star formation histories, ages, and reddening; the latter assumes the Calzetti et al. (2000) attenuation curve, but we consider other attenuation curves below. The photometry is corrected, if necessary, for the contribution from the strongest emission lines measured in our survey, including  $H\alpha$ ,  $H\beta$ ,  $[O\text{ III}]\lambda\lambda 4960, 5008$ , and  $[O\text{ II}]\lambda\lambda 3727, 3730$ . We modeled the stellar populations using constant, declining, and exponentially rising star formation histories with  $e$ -folding times of  $\tau = 100\text{--}5000$  Myr, and generally adopted the exponentially rising histories as the default for reporting results from the fitting. In the case of 14 galaxies, exponentially declining models were adopted because they yielded better fits to the rest-UV photometry. Incorporating the parameters obtained for a constant star formation history does not alter our analysis or conclusions. In the modeling, we allowed the age to vary from 50 Myr (approximately the dynamical timescale; e.g., Reddy et al. 2012b) to the age of the Universe at the redshift of each galaxy. Reddening in the range  $0.0 \leq E(B - V) \leq 0.6$  was considered. We adopted the parameters corresponding to the model that gave a minimum  $\chi^2$  relative to the photometry. Errors in the best-fit parameters were derived by perturbing the photometry assuming a Gaussian distribution of FWHM equal to the photometric uncertainties. Each of these realizations of the photometry were then refit to find the best-fit model, and the errors in best-fit parameters were taken to be the values that encompassed 68% of the simulations.

Of the 259 galaxies in our sample, 35 (31 H $\beta$ -detected and 4 H $\beta$ -undetected) galaxies had noisy photometry relative to the best-fit model and were excluded from subsequent analysis. Thus, the final sample consists of 224 galaxies, with 182 H $\beta$ -detected galaxies and 42 H $\beta$ -undetected galaxies.

### 2.7. Balmer Optical Depth

As in Calzetti et al. (1994), we define the *Balmer optical depth*

$$\tau_b \equiv \ln \left( \frac{H\alpha/H\beta}{2.86} \right). \quad (1)$$

Here,  $\tau_b$  is the *difference* in optical depths measured at the wavelengths of H $\beta$  and H $\alpha$ , with the usual definition:  $\tau_\lambda = -\ln(I_\lambda/I_\lambda^0)$  where  $I_\lambda$  and  $I_\lambda^0$  are the observed and intrinsic intensities, respectively. Thus,  $\tau_b$  is directly related to the color excess,  $E(B - V)$ . Objects with measured H $\alpha$ /H $\beta$  < 2.86, which is the theoretical minimum value in the absence of dust for Case B recombination and  $T = 10,000$  K (Osterbrock 1989), are assigned  $\tau_b = 0$ .<sup>6</sup>

### 2.8. SFR Calculations

The default measurements we use for the SFRs come not from the SED fitting, but from the H $\alpha$  flux measurements. The latter are more immune to the degeneracies inherent in SED modeling, less affected by extinction than the rest-UV, and trace the “instantaneous” SFR. We used the Kennicutt (1998) relation to convert H $\alpha$  luminosities to SFRs, assuming a Chabrier (2003) IMF. These observed SFRs were then corrected for attenuation by assuming an attenuation curve  $k(\lambda)$  and nebular color excess  $E(B - V)_{\text{gas}}$ . In most previous investigations at *high redshift*, the attenuation curve assumed for the nebular line regions is the Calzetti et al. (2000) curve, with color excesses based on those found for the stellar continuum (also assuming a Calzetti et al. 2000 curve). In our analysis, we calculated SFR(H $\alpha$ ) assuming the Cardelli et al. (1989) Galactic extinction curve, as was the original intent of Calzetti et al. (1994), but we explore the effect of assuming other attenuation curves in deriving the color excess, as well as the implications for dust corrections and bolometric SFRs, in Sections 4.3 and 4.4. Throughout the paper, and unless noted otherwise, the specific SFRs (sSFRs) are computed assuming the dust-corrected SFRs(H $\alpha$ ) and the SED-determined stellar masses. This approach is more advantageous than combining SED-determined SFRs with  $M^*$  because these quantities are highly correlated with each other (i.e., both SFR(SED) and  $M^*$  are constrained by the normalization of the best-fit SED model with the photometry).

## 3. THE EFFECT OF DUST ON THE STELLAR CONTINUUM EMISSION

As noted above, the distribution of H $\alpha$ /H $\beta$  ratios implies the presence of dust in the majority of the objects in our sample. Before considering the level of obscuration required to reproduce the observed Balmer decrements—a step that requires the assumption of an attenuation curve—it is instructive to examine how the galaxy spectral shapes vary

with H $\alpha$ /H $\beta$  ratio. We focus specifically on the sensitivity of the UV spectral slope to dust obscuration, given the large absorption cross-section of dust to UV photons, and the prevalent use of the UV slope as a dust indicator for typical star-forming galaxies at high redshifts. Formally, the UV slope  $\beta$  is defined such that  $f_\lambda \propto \lambda^\beta$ . Note that  $\beta$  is the *observed* UV continuum slope, irrespective of the underlying stellar population. Thus, a galaxy with an older stellar population and a significant contribution of UV flux from stars of spectral type A and later, can exhibit the same spectral slope as a galaxy whose UV continuum is dominated by OB stars and contains significant amounts of dust.

### 3.1. Calculation of the UV Slope

In practice,  $\beta$  can be measured directly from a high S/N spectrum using a number of continuum windows spanning the range 1250–2600 Å, where the windows are designed to exclude regions of strong interstellar/stellar absorption and the 2175 Å dust absorption feature (Calzetti et al. 1994). For most galaxies lacking rest-UV spectroscopic data, as in our case, either broad- and intermediate-band photometry, or the stellar population model that best fits such photometry, can be used to estimate  $\beta$ . We calculated a “photometric” UV slope ( $\beta_{\text{phot}}$ ) by fitting the photometry directly (taking into account the photometric errors), which includes for all objects in our sample anywhere from 4 to 19 photometric points that lie in the (rest-frame) range  $\lambda = 1250\text{--}2600$  Å. The measurement uncertainty in the rest-UV photometry results in best-fit UV slopes with a typical error of  $\Delta\beta_{\text{phot}} \simeq 0.2$

For comparison, we also computed an “SED” UV slope ( $\beta_{\text{SED}}$ ) by fitting the flux of the best-fit stellar population model as a function of wavelength, using only those flux points that lie within the 10 continuum windows given in Calzetti et al. (1994). The typical formal uncertainty in  $\beta_{\text{SED}}$ , when using the 10 aforementioned windows, is  $\Delta\beta_{\text{SED}} \simeq 0.1$  (not including the systematic error associated with the assumed stellar population model). The two measures of UV slope,  $\beta_{\text{phot}}$  and  $\beta_{\text{SED}}$ , are highly correlated because the stellar population model is fit to the same photometry used to calculate  $\beta_{\text{phot}}$ .

### 3.2. Relation Between UV Slope and Balmer Line Opacity

Our expectation is that if the UV slope is sensitive to dust obscuration, which a number of studies have shown to be the case for different subsets of high-redshift galaxies (e.g., Nandra et al. 2002; Reddy & Steidel 2004; Reddy et al. 2006, 2012a; Daddi et al. 2007; Buat et al. 2009; Pannella et al. 2009; Magdis et al. 2010), then we should observe a correlation between  $\beta$  and  $\tau_b$ . The scatter between these two quantities may hint at other factors that influence  $\beta$ , including star formation history, metallicity of the underlying stellar population, and differences in the geometrical distribution of stars and dust in galaxies.

Figure 2(a) shows the distribution of  $\beta_{\text{phot}}$  with  $\tau_b$  for the 182 objects in our sample with  $S/N_{H\beta} \geq 3$ . The average H $\alpha$ /H $\beta$  ratio for the 42 H $\beta$ -undetected galaxies, as calculated from the composite spectrum (see above), is  $4.1 \pm 0.1$ , corresponding to  $\tau_b = 0.37 \pm 0.02$ . The average value of the *individual*  $\beta_{\text{phot}}$  measurements for these 42 galaxies is  $\beta_{\text{phot}} = -1.00$ . These average values for the H $\beta$ -undetected galaxies are indicated by the star in Figure 2(a). Generally, there is a large dispersion in  $\beta_{\text{phot}}$  at a given Balmer optical depth. In the limit

<sup>6</sup> The intrinsic ratio H $\alpha$ /H $\beta$  is insensitive to the electron density, varying by less than 2% from  $n_e = 10^2$  to  $10^6$  cm<sup>-3</sup>.

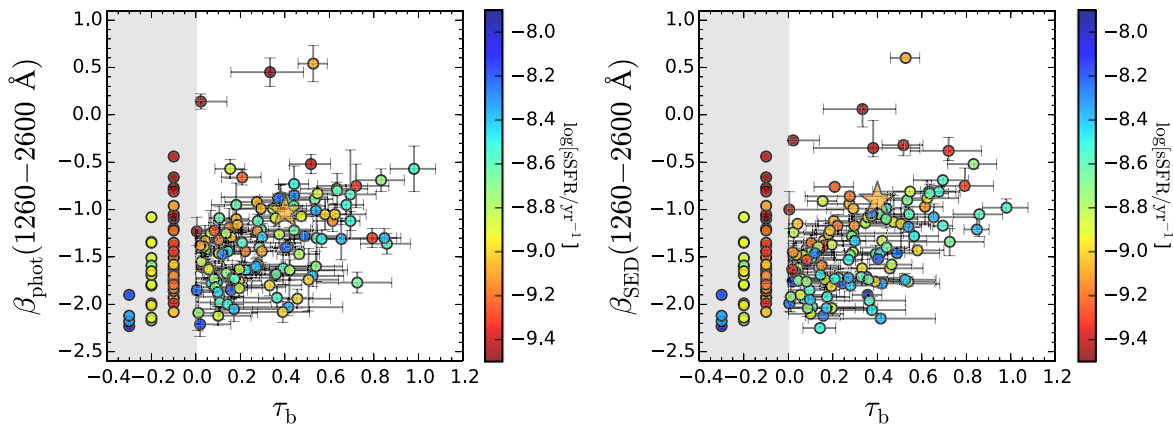


**Figure 2.** Photometric (left;  $\beta_{\text{phot}}$ ) and SED-based (right;  $\beta_{\text{SED}}$ ) UV slopes vs. Balmer optical depth ( $\tau_b$ ), differentiated by sSFR. Errors in  $\tau_b$  include both measurement uncertainties in the  $H\alpha$  and  $H\beta$  fluxes, and the uncertainty in slitloss corrections. Errors in  $\beta_{\text{phot}}$  are derived directly from the linear regression between  $\log f_\lambda$  and  $\lambda$ . Errors in  $\beta_{\text{SED}}$  are estimated from Monte Carlo simulations of the SED fitting (see text). The sSFRs assume dust-corrected  $H\alpha$ -based SFRs and the stellar masses returned from the SED fitting. The large stars indicate the average positions of the  $H\beta$ -undetected galaxies. Galaxies with  $\tau_b = 0$  and different ranges of sSFR are arbitrarily offset to the left side of each panel for clarity.

where  $\tau_b \rightarrow 0$ ,  $\beta$  varies from the bluest ( $\beta_{\text{phot}} \simeq -2.3$ ) to reddest ( $\beta_{\text{phot}} \simeq -0.5$ ) values observed. As noted,  $\beta$  can be sensitive to factors other than the dust content, possibly accounting for some of the scatter in UV slope at a given Balmer optical depth. These factors are discussed in detail below.

### 3.3. Effect of Star Formation History on the UV Slope

#### 3.3.1. Variations with Specific Star Formation Rate

Galaxies with significant older stellar populations can exhibit UV slopes that are redder than those predicted from dust attenuation alone. Specifically, A stars from previous generations of star formation can contribute significantly to the near-UV flux if the current SFR—and hence the contribution from O and B stars—is low, as might be the case for galaxies with low sSFRs. The two consequences of this effect are to increase the scatter in  $\beta$  at a fixed  $\tau_b$ , and to accentuate the trend in  $\beta$  versus  $\tau_b$  if dustier galaxies are on average older and more massive. For the moment, we consider the effect of star formation history (i.e., effect of older stellar populations) on  $\beta$  by color-coding the points in Figure 2 by sSFR. It is apparent that there is a “sequence” in the location of galaxies in the  $\beta_{\text{phot}}-\tau_b$  plane with sSFR, such that the locus of points shifts toward redder  $\beta_{\text{phot}}$  at a fixed  $\tau_b$  with *decreasing* sSFR. This is the expected behavior if late-type stars increasingly affect the near-UV flux with decreasing sSFR. The shifting of the locus is also (unsurprisingly) apparent if we differentiate the points again by sSFR, but use  $\beta_{\text{SED}}$  instead of  $\beta_{\text{phot}}$  (Figure 2).

To quantitatively demonstrate the shifting of the  $\beta$  versus  $\tau_b$  relation with sSFR, we executed two tests. In the first, we used K–S statistical tests to determine the probability that two distributions of  $\beta$  at two given sSFRs (and at a fixed  $\tau_b$ ) are drawn from the same parent distribution. In practice, we gridded the data in three bins of  $\tau_b$  ( $\tau_b = 0$ , 0.0–0.3, and 0.3–1.0), and two bins of  $\log(\text{sSFR}/\text{yr}^{-1})$ , where  $-9.60 \leq \log(\text{sSFR}/\text{yr}^{-1}) \leq -8.84$  and  $-8.84 \leq \log(\text{sSFR}/\text{yr}^{-1}) \leq -8.00$ . The sSFR bin boundaries were chosen to encompass most of the objects in our sample, with an equal number of objects per sSFR bin. We then performed two-sided K–S tests on the two distributions of  $\beta$  (for the two sSFR bins)

**Table 1**  
K–S Test Results<sup>a</sup>

	$\tau_b = 0$	$\tau_b = 0.0\text{--}0.3$	$\tau_b = 0.3\text{--}1.0$
$\beta_{\text{phot}}$	0.06	0.008	0.09
$\beta_{\text{SED}}$	0.05	0.004	0.05

**Note.**

<sup>a</sup> Probability that the distributions of  $\beta$  in the two bins of  $\log(\text{sSFR}/\text{yr}^{-1})$  ( $-9.60 \leq \log(\text{sSFR}/\text{yr}^{-1}) \leq -8.84$  and  $-8.84 \leq \log(\text{sSFR}/\text{yr}^{-1}) \leq -8.00$ ) in the given bins of  $\tau_b$  are drawn from the same parent population.

in each bin of  $\tau_b$ . The results are summarized in Table 1, and suggest that the  $\beta$  distributions between the two sSFR bins are drawn from different parent populations.

In the second test, we divided the data into the same two bins of sSFR defined above, and we computed the Spearman correlation coefficient and the significance with which the null hypothesis of no correlation between  $\beta$  and  $\tau_b$  can be ruled out. Table 2 summarizes the results for  $\beta_{\text{SED}}$  versus  $\tau_b$  and  $\beta_{\text{phot}}$  versus  $\tau_b$ . Significant correlations between  $\beta$  and  $\tau_b$  are found in most cases, with the slopes and intercepts from linear regressions indicated in Table 2. We also estimated the intrinsic dispersion in the data ( $\sigma_{\text{int}}$ ) by assuming that the total dispersion in  $\beta$  versus  $\tau_b$  is the quadrature sum of  $\sigma_{\text{int}}$  and the measurement error,  $\sigma_{\text{meas}}$ . Clearly,  $\sigma_{\text{int}}$  will depend on the adopted bin widths, but our goal was to determine the degree to which the  $\beta - \tau_b$  correlations in given sSFR bins overlap when considering the intrinsic scatter in the data. The fits obtained for  $\beta_{\text{SED}}$  versus  $\tau_b$  are shown in Figure 3. From these statistical tests, it is clear that the scatter seen in Figure 2 is to a large extent due to variation in the  $\beta$  versus  $\tau_b$  relations for galaxies with different sSFRs. Specifically, the relation for the lowest sSFR galaxies is shifted to redder  $\beta$  by  $\approx 2 \times \sigma_{\text{int}}$  relative to the relation for the highest sSFR galaxies.

#### 3.3.2. Contribution of A Stars to the Near-UV Flux

We have shown that galaxies with lower sSFRs have on average redder UV slopes at a given Balmer optical depth, but it remains to be seen whether late-type stars are responsible for this trend. To assess the contribution of lower mass A stars to

**Table 2**  
Spearman Correlation Test and Linear Regression Results for  $\beta$  vs.  $\tau_b$

$\beta$	$\log[\text{sSFR}/\text{yr}^{-1}]$	$N^a$	$\rho_{\text{Spear}}^b$	$\sigma_{\text{Spear}}^c$	Slope	Intercept	$\sigma_{\text{rms}}^d$	$\sigma_{\text{int}}^e$
$\beta_{\text{phot}}$	-9.60...-8.84	87	0.33	3.12	$0.57 \pm 0.15$	$-1.42 \pm 0.02$	0.52	0.33
...	-8.84...-8.00	87	0.56	5.24	$0.73 \pm 0.11$	$-1.67 \pm 0.03$	0.38	0.21
$\beta_{\text{SED}}$	-9.60...-8.84	87	0.55	4.42	$0.95 \pm 0.14$	$-1.48 \pm 0.02$	0.47	0.31
...	-8.84...-8.00	87	0.65	6.07	$0.87 \pm 0.09$	$-1.78 \pm 0.03$	0.33	0.20

**Notes.**

<sup>a</sup> Number of galaxies.

<sup>b</sup> Spearman rank correlation coefficient.

<sup>c</sup> Standard deviations from null hypothesis.

<sup>d</sup> Total rms.

<sup>e</sup> Intrinsic dispersion (see text).

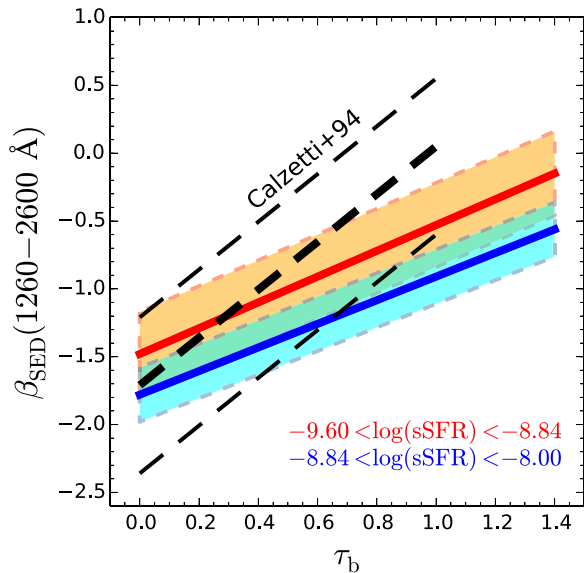


**Figure 3.** Linear regressions between  $\beta_{\text{SED}}$  and  $\tau_b$ . The solid lines and shaded regions indicate the best-fit linear functions and estimated  $\pm\sigma_{\text{int}}$  intrinsic scatter for the different bins of sSFR, respectively. Individual data points have been omitted for clarity. Long-dashed lines indicate the best-fit linear function and upper and lower envelopes from Calzetti et al. (1994) for a sample of 39 local starburst and blue compact galaxies (Kinney et al. 1993).

the UV continuum, we recalculated the UV slopes using only those photometric points that lie blueward of rest-frame 1750 Å,  $\beta(1260-1750 \text{ \AA})$ . Only O and B stars, and the most massive A stars (spectral type A1, A0) contribute significantly at these blue wavelengths (e.g., Calzetti et al. 1994; Leitherer & Heckman 1995). We compared these “blue” UV slopes to those obtained using photometry over the full wavelength range between 1260 and 2600 Å,  $\beta(1260-2600 \text{ \AA})$ . The comparison (Figure 4) includes only those galaxies that had a minimum of four photometric points available for calculating  $\beta$  when excluding all points with  $\lambda > 1750 \text{ \AA}$ .<sup>7</sup>

We find no evidence that galaxies with lower sSFRs have  $\beta_{\text{phot}}(1260-1750 \text{ \AA})$  bluer than  $\beta_{\text{phot}}(1260-2600 \text{ \AA})$ , as would be expected if the near-UV continua of such galaxies were

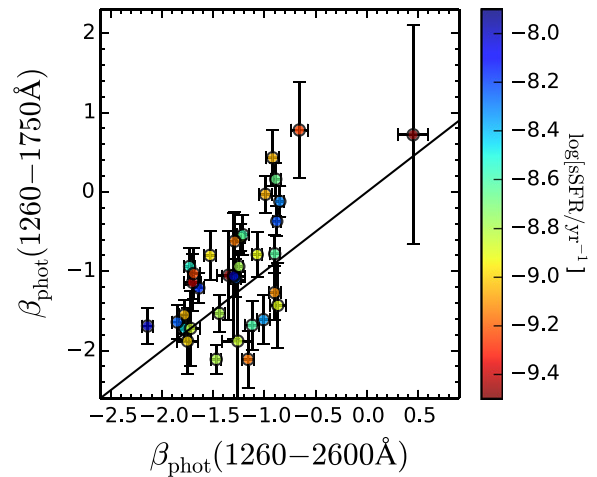


**Figure 4.** Comparison of UV spectral slopes computed over different wavelength ranges that include ( $\beta_{\text{phot}}(1260-2600 \text{ \AA})$ ) and exclude ( $\beta_{\text{phot}}(1260-1750 \text{ \AA})$ ) the near-UV portion of the spectrum that can have a significant contribution from stars of A2 and later spectral types. We find no evidence that  $\beta_{\text{phot}}(1260-1750 \text{ \AA})$  is systematically bluer than  $\beta_{\text{phot}}(1260-2600 \text{ \AA})$ , suggesting that A stars do not contribute significantly to the near-UV continuum, even for galaxies with lower sSFRs.

weighted more heavily by the flux from A stars. The same conclusion is reached when considering the relation between  $\beta_{\text{phot}}(1260-1750 \text{ \AA})$  and the slope obtained using photometry that is strictly in the near-UV,  $\beta_{\text{phot}}(1750-2600 \text{ \AA})$ .

The redness of the UV slope measured over the shorter baseline in wavelength can in principle reflect the more severe attenuation at these short wavelengths, which is an issue that we discuss briefly in Section 4.2. Because the difference between  $\beta$  measured across the short and long wavelength baselines does not appear to correlate with sSFR (Figure 4), the contribution of older stars to the near-UV continuum is likely minimal over the range of sSFR considered here, and thus not a dominant factor in the spread or trend in  $\beta$  with  $\tau_b$ .

### 3.4. Effect of Metallicity on the UV Slope

An issue separate from the effect of older stars on the near-UV continuum is the extent to which differences in metallicities of the stellar populations lead to trends between  $\beta$  and  $\tau_b$ . We investigated the dependence of  $\beta$  on metallicity by using MOSDEF measurements of the  $[\text{N II}]\lambda 6585/\text{H}\alpha$  ratio

<sup>7</sup> The galaxies shown in Figure 4 are all in the COSMOS field, where  $\beta$  is determined using both broad- and intermediate-band photometry with sufficient independent wavelength sampling to accurately compute the UV slope in the relevant wavelength ranges.

(“N2 index”) with the Pettini & Pagel (2004) calibration to infer the gas-phase oxygen abundance.<sup>8</sup> We have assumed that the gas-phase and stellar metallicities track each other closely, as should be the case for the short-lived O and B stars that dominate the UV continuum. The range of metallicities probed by our sample is  $8.1 \lesssim 12 + \log(\text{O}/\text{H}) \lesssim 8.7$  (i.e.,  $0.2 \lesssim Z \lesssim 1.0 Z_{\odot}$ , assuming the value of the solar abundance from Allende Prieto et al. 2001 and Asplund et al. 2004), with a mean oxygen abundance that changes by  $\simeq 0.3$  dex between the reddest and bluest UV slopes. For a Chabrier (2003) IMF and a constant star formation for 100 Myr, the Bruzual & Charlot (2003) stellar population synthesis models imply a difference in intrinsic UV slope of  $\Delta\beta_{\text{int}} \simeq 0.2$  for the range of metallicities probed in our sample. This difference is much smaller than the spread in  $\beta$  at a given  $\tau_b$ , and much smaller than the change in  $\beta$  as  $\tau_b$  increases (Figure 2). We conclude that differences in the metallicities of the stellar populations are unlikely to be the dominant factor in driving the change in UV slope with increasing Balmer line opacity.

### 3.5. Scatter in $\beta$ in the Limit where $\tau_b \rightarrow 0$

The previous discussion of the effects of late-type stars and metallicity on the UV slope leads to the conclusion that dust obscuration is likely the underlying cause of the trend between  $\beta$  and Balmer optical depth. In this scheme, variations in the dust opacity between individual galaxies are likely responsible for the scatter in  $\beta$  at a fixed  $\tau_b$ . Such variations in the opacity may be due to a dependence on dust composition, resulting in different absorption and scattering cross-sections of the dust grains. Alternatively, the geometrical distribution of the dust with respect to the ionizing stars in galaxies can lead to variations in dust opacity. Galaxies of a given  $\tau_b$  may exhibit a wide range of  $\beta$  depending on the dust column densities toward the ionized regions and the stellar continuum (e.g., Calzetti et al. 1994, 2000). Although, as emphasized in Calzetti et al. (1994), the spatial distribution of dust and stars cannot explain the large scatter in  $\beta$  in the limit where  $\tau_b \rightarrow 0$ . In this limit, we expect  $\beta$  to approach its intrinsic value, typically between  $\beta_{\text{int}} \simeq -2.6$  and  $-2.0$ , depending on the details (e.g., IMF, metallicity) of the stellar population model.

There are several reasons to suspect that galaxies with  $\tau_b = 0$  are not dust-free, even though their Balmer decrements would indicate formally otherwise. First, such galaxies have measurement errors in  $\tau_b$  that do not exclude the presence of some dust. Second, even galaxies with the bluest UV spectral indices in our sample have metallicities of at least  $12 + \log(\text{O}/\text{H}) \gtrsim 8.1$  ( $\simeq 0.26 Z_{\odot}$ ), implying that they must contain some dust. Third, if we de-redden the best-fit SEDs assuming a Calzetti et al. (2000) attenuation curve and the best-fit  $E(B - V)$ , we obtain  $\beta_{\text{int}} \simeq -2.3$ . This is significantly bluer than the  $\beta_{\text{int}} \simeq -1.3$  and  $-1.6$  implied by the linear regression for the bin of lowest sSFR (Table 2). Moreover, the detection of H $\alpha$  emission in these galaxies requires the presence of hydrogen-ionizing stars, and the blue hot stars will cause an otherwise intrinsically shallow UV spectral index to become steep (i.e., more negative). Finally, from an observational standpoint, if the rest-UV emission in these galaxies is not spatially coincident with the rest-optical emission, then the observed Balmer

decrement may not be indicative of the global reddening of the galaxy as deduced from the UV slope, which is a case that may apply for all galaxies in our sample. For these reasons, the linear regressions between  $\beta$  and  $\tau_b$  should be interpreted with caution in the limit  $\tau_b \rightarrow 0$ .

To summarize, the results of Section 3.3.1 (e.g., Figures 2 and 3) imply that the physical origin of the scatter in  $\beta$  versus  $\tau_b$  must vary systematically with sSFR, a point that we discuss further in the next section. We have investigated the potential effect of A stars on our measurements of  $\beta$  and find that it cannot explain the scatter in  $\beta$  at a given  $\tau_b$ . Further, variations of the high-mass end of the IMF (e.g., as a function of metallicity) lead to corrections of the UV slope of  $\approx 10\%$  (Calzetti et al. 1994), which again cannot account for the large scatter in  $\beta$  at a given  $\tau_b$ . In Section 4, we put forth a physical interpretation that is consistent with the trends and scatter between  $\beta$  and  $\tau_b$ .

### 3.6. The Attenuation Curve of High-redshift Galaxies

Given evidence that neither an older stellar population nor a change in metallicity is responsible for the reddening of  $\beta$  with increasing  $\tau_b$ , we are left with the possibility that dust attenuation is the dominant factor in the observed trend between  $\beta$  and  $\tau_b$ . A similar line of reasoning is presented in Calzetti et al. (1994) to account for the correlation between UV slope and Balmer optical depth for a sample of 39 local starburst and blue compact galaxies from Kinney et al. (1993), where the local trend is shown in Figure 3. Interestingly, we find that the correlation between UV slope and Balmer optical depth is steeper for the local sample, relative to that observed for the  $1.4 \lesssim z \lesssim 2.6$  MOSDEF sample. The median sSFR of the local galaxies is  $\log(\text{sSFR}/\text{yr}^{-1}) \approx -9.00$ , and these galaxies generally have both lower SFRs ( $\simeq 4 M_{\odot} \text{yr}^{-1}$ ) and lower stellar masses ( $\simeq 3.9 \times 10^9 M_{\odot}$ ) compared to those in our sample. A more detailed comparison of our results with local samples (including the SDSS) will be presented elsewhere. For the moment, we note that the segregation of the  $\beta$  versus  $\tau_b$  relations (Figure 3) indicates an sSFR-dependent scaling between nebular and stellar attenuation in high-redshift galaxies that differs from local ones (Section 3.6.2).

#### 3.6.1. Derivation of the Selective Attenuation Curve

In what follows, we adopt a procedure similar to that presented in Calzetti et al. (1994), generalized from that of Kinney et al. (1994), to derive the selective attenuation curve. The premise behind this procedure is that because the UV spectral index is sensitive primarily to dust attenuation, the ratio of the average spectrum of galaxies with high Balmer optical depths to that of galaxies with low optical depths should reflect the average effect of attenuation on the stellar SEDs. Of course, especially in the optical and near-IR, there can be a wide range of intrinsic SED shapes for star-forming galaxies depending on their star formation histories and ages. However, to first order, galaxies of a given sSFR will have comparably shaped intrinsic stellar SEDs, as the flux at any given wavelength is contributed to in a similar proportion by the current star formation and the light from previous generations of star formation. The exact form of how the previous stellar mass was built up (i.e., the star formation history) is unimportant, as the rest-frame optical to near-IR light that is used to infer stellar masses (and hence sSFRs) arises from

<sup>8</sup> A discussion of the different metallicity indicators accessible with MOSDEF are discussed in Sanders et al. (2015). Assuming these different indicators does not alter our conclusions regarding the change in  $\beta$  with inferred oxygen abundance.

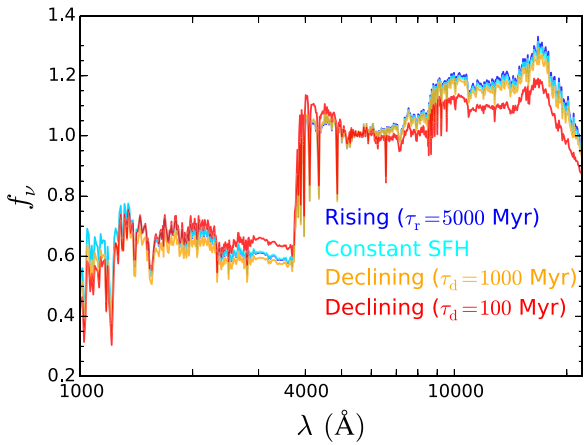


**Figure 5.** Stellar SEDs for a galaxy with a stellar mass of  $M^* \simeq 1.2 \times 10^{10} M_\odot$  and  $\text{SFR} \simeq 16 M_\odot \text{yr}^{-1}$ , assuming different simple star formation histories: an exponentially rising model with an  $e$ -folding time of 5000 Myr, constant star formation, and exponentially declining models with  $e$ -folding times of 1000 and 100 Myr. The corresponding ages of the stellar populations are  $\approx 800$ , 3000, 720, 570, and 200 Myr, respectively. The SEDs are cast in terms of  $f_\nu$  and are normalized so that  $f_\nu(\lambda = 5500 \text{ \AA}) = 1$ . Fixing the sSFR of the galaxy results in similar SED shapes for most of the assumed star formation histories.

some combination of the *currently* forming stellar population, and from lower mass (spectral type F5 and later) stars that have not yet evolved off the main sequence for the age of the Universe at  $z \sim 2$ .<sup>9</sup> For instance, Figure 5 shows the conformity of the stellar SED for a galaxy with an SFR and  $M^*$  (and hence, sSFR) typical of the average galaxy in our sample, irrespective of the star formation history. SEDs that assume a relatively short decay timescale for star formation (e.g.,  $\tau_d \lesssim 100$  Myr) deviate by  $\approx 10\%$  at optical and near-IR wavelengths, but such histories are ruled out for the vast majority of objects in our sample given their typical stellar population ages of  $\gtrsim 300$  Myr, combined with the evidence that, at least on average,  $>L^*$  galaxies at  $z \sim 2$  show evidence for rising star formation at previous epochs (e.g., Reddy et al. 2012b).

Motivated by the apparent sSFR-dependence of the  $\beta$  versus  $\tau_b$  relation, we derived the attenuation curve for galaxies in two bins of sSFR. We first examined the distribution of sSFR with  $\tau_b$  (Figure 6). Approximately 96% of the galaxies in our sample (174 of 182) lie in the range  $-9.6 \leq \log[\text{sSFR}/\text{yr}^{-1}] < -8.0$ . Dividing the number of objects in this range into two bins, with equal numbers of objects (87) per bin, results in the following sSFR bins:  $-9.60 \leq \log[\text{sSFR}/\text{yr}^{-1}] < -8.84$  (sSFR bin 1) and  $-8.84 \leq \log[\text{sSFR}/\text{yr}^{-1}] < -8.00$  (sSFR bin 2). The objects within each sSFR bin were further divided into three bins of  $\tau_b$ . For sSFR bin 1, the first  $\tau_b$  bin includes all objects with  $\tau_b = 0$ , and the remaining objects are split roughly equally into two additional bins. Given the low number of objects (eight) that have  $\tau_b = 0$  in sSFR bin 2, for this sSFR bin we divided the objects equally into three bins of  $\tau_b$ .

<sup>9</sup> This assumes an IMF that does not evolve with redshift above  $z \sim 2$ . Some circumstantial evidence for an un-evolving IMF at  $z \gtrsim 2$  comes from the general agreement between the integral of the cosmic SFR density and the evolution of the stellar mass density (Reddy & Steidel 2009; Madau & Dickinson 2014).

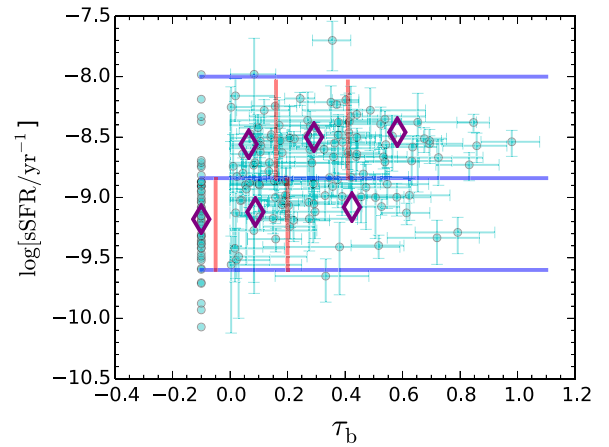


**Figure 6.** Distribution of sSFR with Balmer optical depth. Objects with  $\tau_b = 0$  are offset to the left for clarity. The horizontal lines denote the boundaries of the two sSFR bins and the vertical lines denote the boundaries of the three  $\tau_b$  bins per sSFR bin used to calculate the attenuation curve. The open diamonds indicate the mean values of  $\log[\text{sSFR}/\text{yr}^{-1}]$  and  $\tau_b$  for each bin.

The derivation of the attenuation curve relies on the assumption that the *average* intrinsic SED (and hence the sSFR) is unchanging as a function of Balmer optical depth, regardless of the exact mix of different star formation histories that may be contributing to that average SED. Figure 6 shows that the average sSFRs of galaxies in each bin of  $\tau_b$  is roughly constant, implying that a simple ratio of the average SEDs obtained in each bin will directly probe the wavelength dependence of dust obscuration. In Section 3.6.4, we address the slight ( $< 0.1$  dex) differences in the  $\langle \log[\text{sSFR}/\text{yr}^{-1}] \rangle$  obtained in each bin, and how these differences translate into a systematic uncertainty in our derived attenuation curve.

Having established the aforementioned bin definitions, we then estimated the average SED of objects in each bin as follows. The broad- and intermediate-band fluxes measured for each object were normalized by the flux of the best-fit SED for that object at rest-frame  $\lambda = 5500 \text{ \AA}$  and then shifted to the rest-frame based on its spectroscopic redshift. The normalized flux density measurements for all objects were then combined and fit with a Bruzual & Charlot (2003) stellar population model. In the fitting, we assumed an equal weighting for all objects irrespective of the flux measurement errors, so that no single object dominated the fit, although we note that taking into account photometric errors results in fits that are similar to those obtained here. To ensure the best possible fit to the data, we allowed for a range of possible star formation histories (declining, constant, and rising), no restriction on the age of the model apart from it being less than the age of the Universe at the mean redshift of the sample  $\langle z \rangle \sim 2.0$ , color excesses from  $E(B - V) = 0.00$  to 0.60, as well as four attenuation curves, a Calzetti starburst reddening curve (Calzetti et al. 2000), and the line-of-sight SMC, LMC, and Galactic extinction curves. The exact details of the best-fit model are not essential, so long as the model provides a good fit to the fluxes of the contributing objects. Figure 7 shows the best-fit functional form to the normalized photometry of all objects in each bin of sSFR and  $\tau_b$ . In this regard, also shown are the weighted mean fluxes of objects in 1000  $\text{\AA}$ -width bins in wavelength (i.e., the empirical SED), demonstrating that the model fits are not in any way skewed relative to these mean empirical values. Below, we also

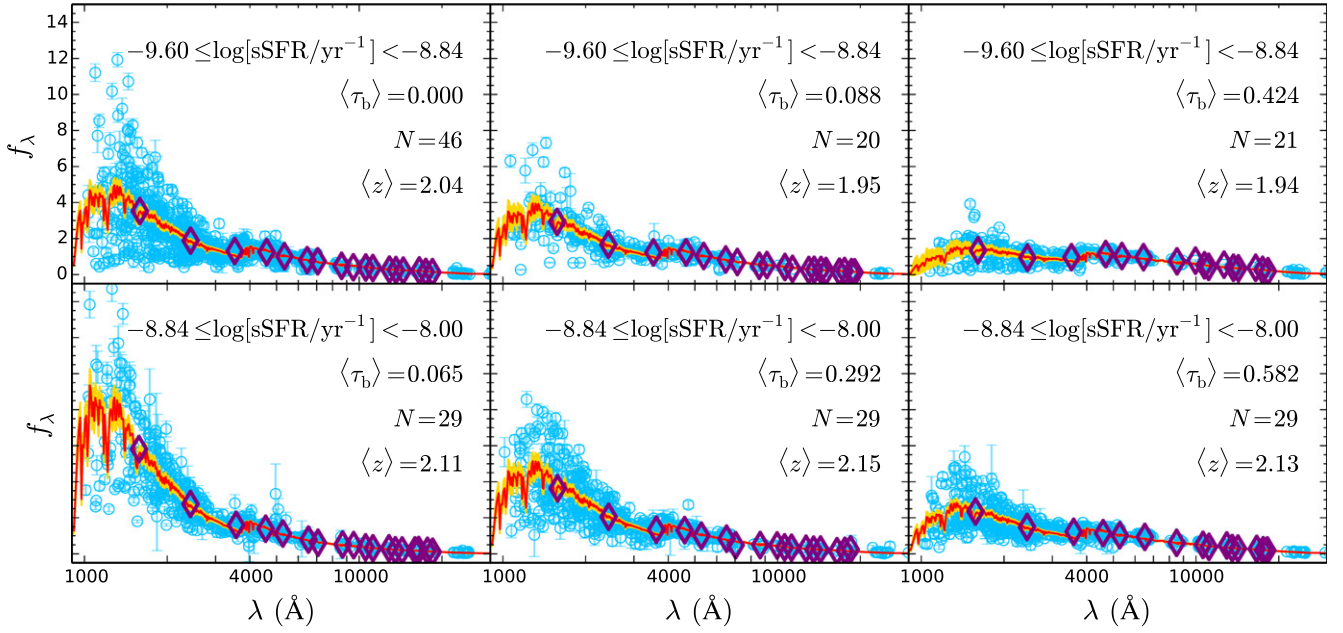


**Figure 7.** Photometry (circles) and model fits (red) of objects in bins of sSFR and Balmer optical depth, with the number of contributing objects and mean redshifts indicated. The photometry has been normalized such that  $f_\lambda(5500 \text{ \AA}) = 1$ . The fitting takes into account the photometric (flux) errors and allows for a range of possible star formation histories, ages, color excesses, and attenuation curves (see text). The orange shaded regions indicate the  $1\sigma$  dispersion about the mean SED fits, based on Monte Carlo simulations where the sSFRs,  $\tau_b$ , and photometric errors for each object are perturbed and the mean SED is recalculated. For comparison, the diamonds show the unweighted average of the fluxes in  $1000 \text{ \AA}$ -width bins in wavelength.

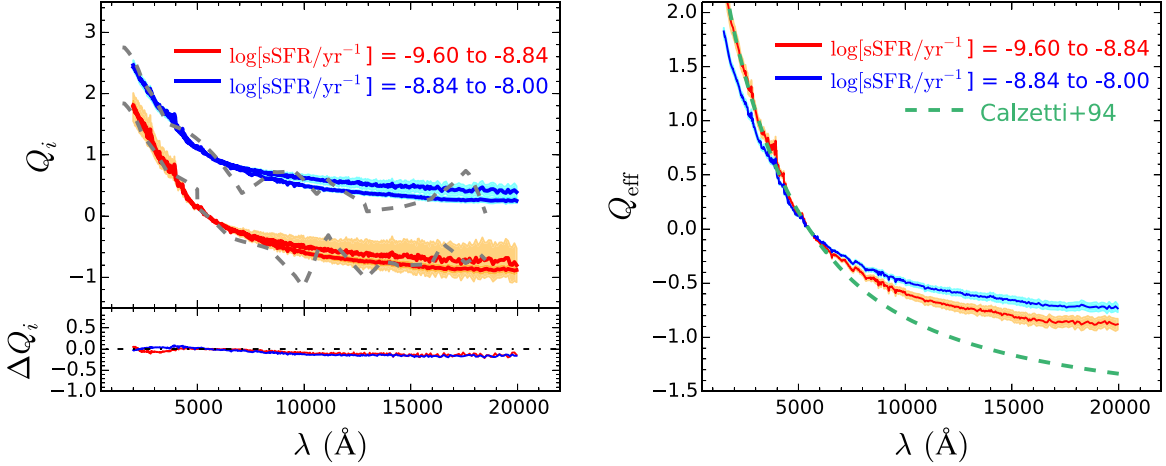


**Figure 8.** Left: selective attenuation curves ( $Q_2$  and  $Q_3$ ) calculated using objects in two bins of sSFR. The curves for sSFR bin 2 have been shifted upward by  $\Delta Q_i = 1$  for clarity. The shaded regions indicate the uncertainties in  $Q_i$ . The  $Q_i$  inferred from the empirical SEDs are denoted by the dashed lines. Also shown at the bottom is the difference between  $Q_3$  and  $Q_2$  as a function of wavelength for each bin of sSFR. Right: effective attenuation curves ( $Q_{\text{eff}}$ ) calculated as the weighted average of the  $Q_2$  and  $Q_3$  shown in the left panel for each sSFR bin. The weighted uncertainties in  $Q_{\text{eff}}$  are indicated by the shaded regions. The dashed line shows the Calzetti et al. (1994) selective attenuation curve.

demonstrate that our model fits result in a shape of the attenuation curve that follows the one calculated from the empirical SEDs.

The random uncertainty in the average SEDs was estimated as follows. For each object, we perturbed its sSFR and  $\tau_b$  based on the errors in these quantities, and then rebinned all the objects according to these perturbed values. The photometry of each object was also perturbed according to the photometric errors, and the average SEDs were recalculated. This procedure was repeated 100 times to obtain statistically robust

determinations of the standard deviations in the average SEDs, which are shown by the shaded regions in Figure 7.

The *selective attenuation* between each of these average (composite) SEDs is then defined as

$$Q_i(\lambda) \equiv -\frac{1}{\tau_i - \tau_1} \ln \left[ \frac{F_i(\lambda)}{F_1(\lambda)} \right], \quad (2)$$

where  $\tau_i$  and  $F_i$  refer to the average Balmer optical depth and the composite spectrum, respectively, of the objects in the  $i$ th

bin of  $\tau_b$  (Calzetti et al. 1994).  $Q_i$  is computed relative to the first bin, whereby construction  $\tau_1 = 0$  for the first sSFR bin, and  $\tau_1 = 0.065$  for the second sSFR bin. Thus, for each bin of sSFR, we obtain two estimates of the selective attenuation ( $Q_2$  and  $Q_3$ ). Figure 8 shows our calculation of  $Q_2$  and  $Q_3$  for the two bins of sSFR specified above. The uncertainties in  $Q_i$  were determined by randomly perturbing the composite SEDs according to their respective uncertainties and recomputing  $Q_i$  for these realizations. The errors in the mean  $Q_i$  are indicated by the shaded regions in Figure 8, and are  $\sigma(Q_2) \approx 0.20$  and  $\sigma(Q_3) \approx 0.05$  for sSFR bin 1, and  $\sigma(Q_2) \approx 0.10$  and  $\sigma(Q_3) \approx 0.04$  for sSFR bin 2. The differences between  $Q_2$  and  $Q_3$  for a given sSFR bin are  $\Delta Q_i \lesssim 0.15$ , or  $\lesssim 0.07$  dex, and are of the same order as the random uncertainties in the mean  $Q_i$ .

Additionally, we calculated the  $Q_i$  based on the empirically determined SEDs. This was accomplished by linearly interpolating between the average flux points of each composite SED (i.e., as shown by the diamonds in Figure 7) to produce an empirical SED. These empirical SEDs were then combined in the same way as the model fits in order to calculate  $Q_i$  (i.e., using Equation (2)), and the results are denoted by the dashed lines in the left panel of Figure 8 (for clarity, we show the results for  $Q_3$ ). The empirically determined  $Q_i$  track closely those inferred from our model fits, and for our subsequent analysis, we adopt the latter.

Our analysis indicates that the  $Q_i$  within a given sSFR bin are very similar in shape, implying that the average SEDs used to compute  $Q_i$  have roughly similar stellar populations (as would be expected given the previous discussion regarding the similarity in SED shapes for a given sSFR). In other words, the shape of  $Q_i$  is dictated primarily by differences in the dust obscuration, as parameterized by  $\tau_b$ , between the average SEDs shown in Figure 7, and not by significant differences in the average intrinsic stellar populations from one  $\tau_b$  bin to another (see Section 3.6.4 for a full discussion of the systematic uncertainties in the attenuation curve). Given the similarity in the shapes of  $Q_2$  and  $Q_3$  for each sSFR bin, we simply took a weighted average of the two selective attenuation curves to produce what we refer to as the “effective” attenuation curve,  $Q_{\text{eff}}$ . The weights were calculated as  $1/\sigma_\lambda^2$ , where  $\sigma_\lambda$  is the uncertainty in  $Q_i$  as a function of wavelength. The uncertainty in the weighted average is  $\sigma_{\text{weighted},\lambda} = \sqrt{1/\sum\sigma_\lambda^2}$ .

We fit the effective attenuation curve in each sSFR bin using third-order polynomial functions of  $1/\lambda$  over the wavelength ranges  $\lambda = 0.15\text{--}0.60$  and  $\lambda = 0.60\text{--}2.20$   $\mu\text{m}$ . These specific ranges were chosen to ensure the best possible representation of the data using polynomials of the smallest order. The polynomial fit for sSFR bin 1 ( $-9.60 \leq \log[\text{sSFR}/\text{yr}^{-1}] < -8.84$ ) is:

$$\begin{aligned} Q_{\text{eff}}(\lambda, -9.60 \leq \log[\text{sSFR}/\text{yr}^{-1}] < -8.84) \\ &= -2.101 + 1.450/\lambda - 0.181/\lambda^2 + 0.010/\lambda^3, \\ &\quad 0.15 \leq \lambda < 0.60 \mu\text{m}; \\ &= -0.955 - 0.169/\lambda + 0.732/\lambda^2 - 0.200/\lambda^3, \\ &\quad 0.60 \leq \lambda < 2.20 \mu\text{m}. \end{aligned} \quad (3)$$

The polynomial fit for sSFR bin 2 ( $-8.84 \leq \log[\text{sSFR}/\text{yr}^{-1}] < -8.00$ ) is:

$$\begin{aligned} Q_{\text{eff}}(\lambda, -8.84 \leq \log[\text{sSFR}/\text{yr}^{-1}] < -8.00) \\ &= -1.834 + 1.299/\lambda - 0.179/\lambda^2 + 0.010/\lambda^3, \\ &\quad 0.15 \leq \lambda < 0.60 \mu\text{m}; \\ &= -0.878 + 0.136/\lambda + 0.348/\lambda^2 - 0.091/\lambda^3, \\ &\quad 0.60 \leq \lambda < 2.20 \mu\text{m}. \end{aligned} \quad (4)$$

The error in  $Q_{\text{eff}}$  at each wavelength point was used to weight the data appropriately in the fitting. The formal uncertainty in the model fit at each wavelength varies in the range  $\sigma_{\text{fit}} \approx 0.001\text{--}0.004$ . As discussed in the following, several additional steps are required to convert  $Q_{\text{eff}}$  to a *total* attenuation curve, the reason being that the former is computed using galaxies of different luminosities at different redshifts, and therefore the normalization of the attenuation curve must be determined separately. Nonetheless,  $Q_{\text{eff}}$  is useful in two respects: it indicates the wavelength dependence of the obscuration of the stellar continuum and the optical depth to dust of the continuum relative to the Balmer lines. We discuss these points below.

### 3.6.2. Comparison of the Average Optical Depths of the Continuum and the Balmer Lines

The definition of  $Q_{\text{eff}}$  (Equation (2)) implies that the Balmer optical depth,  $\tau_b$ , is related to the difference in optical depths of the continuum at the wavelengths of H $\beta$  and H $\alpha$ :  $\tau_c(\text{H}\beta) - \tau_c(\text{H}\alpha) = [Q_{\text{eff}}(\text{H}\beta) - Q_{\text{eff}}(\text{H}\alpha)]\tau_b$  (e.g., Calzetti et al. 1994), assuming that  $\langle \tau_b \rangle = 0$  for the first bin of  $\tau_b$ . According to Equations (3) and (4), we can then write  $\tau_c(\text{H}\beta) - \tau_c(\text{H}\alpha) = (0.42 \pm 0.01)\tau_b$  and  $\approx (0.36 \pm 0.01)\tau_b$  for sSFR bins  $-9.60 \leq \log[\text{sSFR}/\text{yr}^{-1}] < -8.84$  and  $-8.84 \leq \log[\text{sSFR}/\text{yr}^{-1}] < -8.00$ , respectively.<sup>10</sup> Thus, we conclude that analogous to local galaxies (e.g., Fanelli et al. 1988; Calzetti et al. 1994; Mas-Hesse & Kunth 1999; Kreckel et al. 2013), the ionized gas in high-redshift galaxies with stellar masses  $\gtrsim 10^9 M_\odot$  is subject to a higher dust optical depth *on average* than the stellar continuum. Qualitatively, this result is consistent with the average difference in color excess between the gas and stars observed in local star-forming galaxies (Calzetti et al. 2000; Kreckel et al. 2013). We return to this point in Section 4.3, where we investigate in detail the relationship between the total attenuation of the ionized gas and stellar continuum for individual galaxies.

### 3.6.3. Shapes of the Attenuation Curves

The total attenuation curve is defined as

$$k(\lambda) \equiv \frac{A_\lambda}{E(B - V)}, \quad (5)$$

where  $A_\lambda$  is the total magnitude of extinction at wavelength  $\lambda$  and  $E(B - V)$  is the color excess of the stellar continuum. Because  $E(B - V) = A(B) - A(V)$ , we can write  $k(B) - k(V) = 1$ . Thus, we multiplied the effective

<sup>10</sup> The relation is only approximate for the bin where  $-8.84 \leq \log[\text{sSFR}/\text{yr}^{-1}] < -8.00$  because the average Balmer optical depth for the bin of lowest  $\tau_b$  is not exactly zero.

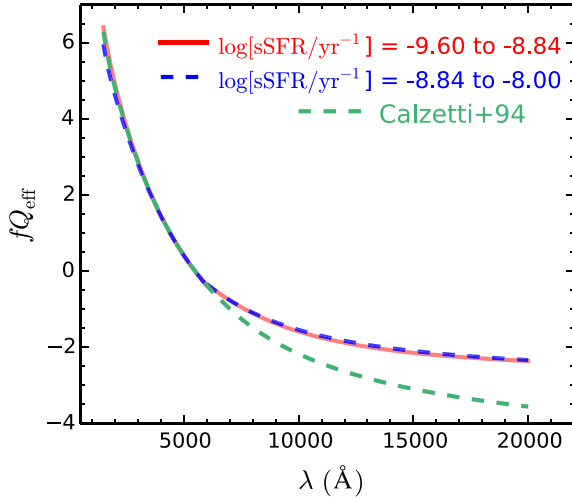


**Figure 9.**  $fQ_{\text{eff}}$  for the two bins of sSFR as indicated in the figure, where the multiplicative factors  $f = 2.676$  and  $3.178$  are required to ensure that  $f[Q_{\text{eff}}(B) - Q_{\text{eff}}(V)] = k(B) - k(V) = 1$  (see text). The Calzetti et al. (1994) attenuation curve is shown for comparison, where we have applied a similar factor  $f \approx 2.659$  (Calzetti et al. 2000).

attenuation curves  $Q_{\text{eff}}$  by the factors  $f = 2.676$  and  $3.178$  for sSFR bins 1 and 2, respectively, so that

$$f[Q_{\text{eff}}(B) - Q_{\text{eff}}(V)] = k(B) - k(V) = 1. \quad (6)$$

The factors were computed by evaluating the effective attenuation curves in the  $B$  ( $\lambda = 4400 \text{ \AA}$ ) and  $V$  ( $\lambda = 5500 \text{ \AA}$ ) bands. The resulting  $fQ_{\text{eff}}$  are shown for the two bins of sSFR in Figure 9.

The two notable aspects of the effective attenuation curves derived here are that (a) they appear to deviate at long wavelengths relative to the Calzetti et al. (1994) selective attenuation curve, and (b)  $Q_{\text{eff}}$  for the two sSFR bins are strikingly similar. On the latter point, a priori we would not have expected such a good agreement given the disparity in the trend of the UV slope with the Balmer optical depth for galaxies with different sSFRs (Section 3.3.1). We return to this issue in Section 4.3. Given the similarity in  $Q_{\text{eff}}$  derived for the two sSFR bins, we simply averaged them, resulting in the following functional form for the *total* attenuation curve:

$$\begin{aligned} k(\lambda) &= -5.726 + 4.004/\lambda - 0.525/\lambda^2 + 0.029/\lambda^3 + R_V, \\ &0.15 \leq \lambda < 0.60 \mu\text{m}; \\ &= -2.672 - 0.010/\lambda + 1.532/\lambda^2 - 0.412/\lambda^3 + R_V, \\ &0.60 \leq \lambda < 2.20 \mu\text{m}; \end{aligned} \quad (7)$$

where  $R_V$  has the usual definition as the ratio of total-to-selective absorption at  $V$ -band:  $R_V = A_V/E(B - V)$ . The last step in the derivation of the total attenuation curve is to calculate  $R_V$ . This can be accomplished by extrapolating  $k(\lambda)$  to some wavelength (e.g.,  $\lambda_n = 2.85 \mu\text{m}$ ) and assuming that  $k(\lambda > \lambda_n) \approx 0$ . This particular value of  $\lambda_n = 2.85 \mu\text{m}$  corresponds to where  $k(\lambda)$  for the SMC, LMC, and Milky Way are very close to zero (Gordon et al. 2003). In our case, if we extrapolate Equation (7) to  $\lambda_n = 2.85 \mu\text{m}$  and force  $k(\lambda_n) = 0$ , then  $R_V = 2.505$ .

Alternatively, a common second approach is to extrapolate  $k(\lambda)$  to infinite wavelength, and set  $k(\lambda \rightarrow \infty) = 0$ . Doing so for Equation (7) results in  $R_V = 2.672$ . More typically, a  $k(\lambda \gg 1 \mu\text{m}) \propto \lambda^{-1}$  dependence is generally assumed. In this case, we determined the functional form of  $k(\lambda > 2.20 \mu\text{m})$  by fitting Equation (7) with a power-law in  $1/\lambda$  in the range  $\lambda = 1.9\text{--}2.2 \mu\text{m}$  (this is to ensure that  $k(\lambda)$  is a continuous function across  $\lambda = 2.2 \mu\text{m}$ ). With this long wavelength extrapolation of  $k(\lambda)$ , and setting  $k(\lambda \rightarrow \infty) = 0$ , we find  $R_V = 2.942$ .

These different extrapolations result in a systematic error in  $R_V$  of  $\approx 0.4$ . Figure 10 shows the comparison of the attenuation curves assuming the smallest and largest values of  $R_V$  derived above, along with several other common extinction and attenuation curves. Independent estimates of  $R_V$  based on mid- and far-IR data will be presented elsewhere. For the remaining analysis, we assumed the first value of  $R_V = 2.505$  because it does not require an extrapolation too far beyond where we have constraints on the shape of the attenuation curve from the photometry ( $\lambda \lesssim 2.2 \mu\text{m}$ ). With this assumption, we arrive at the final expression for the total attenuation curve relevant for the stellar continuum:

$$\begin{aligned} k_{\text{stars}}(\lambda) &= -5.726 + 4.004/\lambda - 0.525/\lambda^2 \\ &\quad + 0.029/\lambda^3 + 2.505, \\ &0.15 \leq \lambda < 0.60 \mu\text{m}; \\ &= -2.672 - 0.010/\lambda + 1.532/\lambda^2 \\ &\quad - 0.412/\lambda^3 + 2.505, \\ &0.60 \leq \lambda < 2.85 \mu\text{m}. \end{aligned} \quad (8)$$

### 3.6.4. Systematic Uncertainty in $k(\lambda)$ Arising from Differences in Average Stellar Populations

As noted previously, the procedure we have used to derive the attenuation curve assumes that the average intrinsic SEDs in the different bins of Balmer optical depth do not vary substantially from one another. Our method of binning the galaxies by sSFR was designed to mitigate any such intrinsic spectral variations. However, while the mean sSFRs as a function of  $\tau_b$  are similar from bin-to-bin (Section 3.6.1 and Figure 6), they are not identical and will therefore introduce some bias in our estimate of the attenuation curve.

To quantify this bias, we first computed an “intrinsic” SED for each galaxy by (a) assuming a rising star formation history with an  $e$ -folding time of  $\tau_r = 5000 \text{ Myr}$  (this is essentially equivalent to assuming a constant star formation history); (b) fixing the stellar mass of the stellar population to be the value derived from the SED fitting (Section 2.6); and (c) varying the age of the stellar population until the corresponding SFR of the model is equal to the (Balmer decrement corrected)  $H\alpha$ -determined one (Section 2.8). The goal of these steps was to construct an SED for a stellar population that had the same sSFR as that computed from  $\text{SFR}(H\alpha)$  and  $M^*$ . Hence, the exact form of the star formation history assumed in step (a) above is inconsequential, as per the discussion in Section 3.6.1.

Second, these intrinsic SEDs were normalized so that  $f(\lambda = 5500 \text{ \AA}) = 1$  and then averaged together for all objects within each bin of sSFR and  $\tau_b$  (assuming the same bins used to derive the attenuation curve). Figure 11 shows these average intrinsic SEDs. The differences in these intrinsic SEDs lead to “correction factors”  $\Delta Q_{\text{int}}$  that must be applied to the  $Q_i$

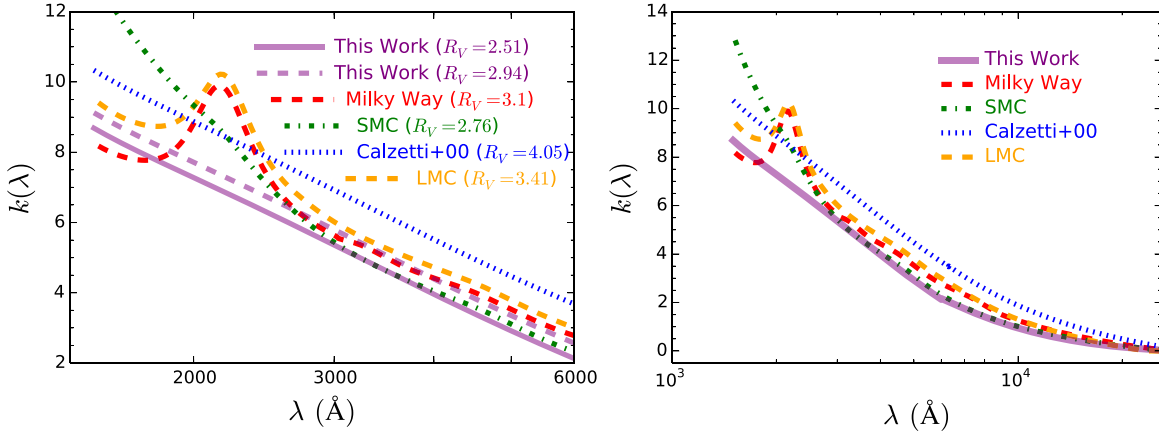


**Figure 10.** Left: comparison of the MOSDEF attenuation curve assuming two different values of  $R_V = 2.505$  and  $R_V = 2.942$  (see text), and that of Calzetti et al. (2000) (dotted line). Also included are the local extinction curves of the Milky Way, SMC, and LMC, where the shapes and normalizations ( $R_V$ ) have been taken from Gordon et al. (2003). Right: same as left panel, where we show the MOSDEF attenuation curve assuming  $R_V = 2.505$  across the full wavelength range  $\lambda = 0.15\text{--}2.50 \mu\text{m}$ .

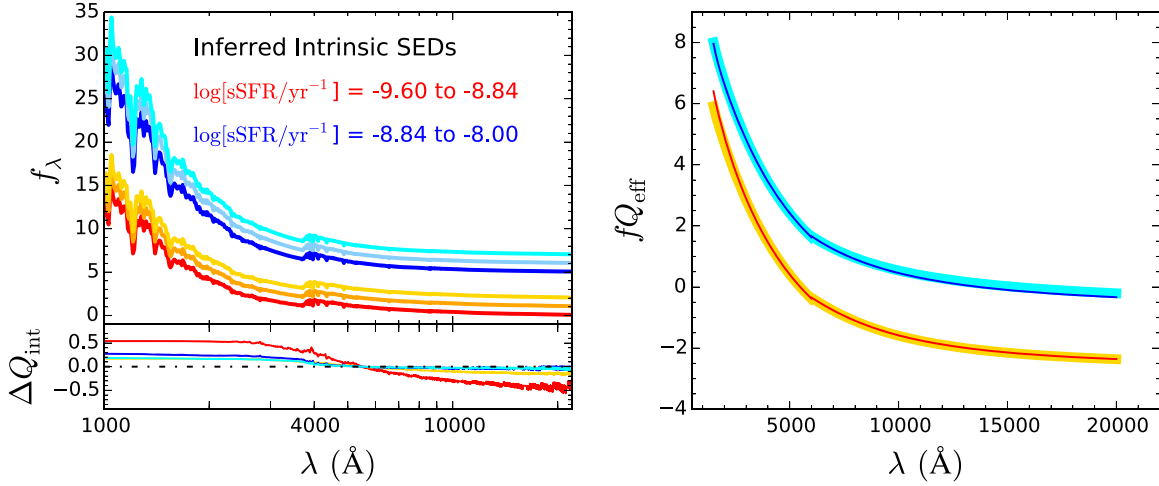


**Figure 11.** Left: inferred average intrinsic SEDs for the same bins of sSFR and  $\tau_b$  used to calculate the attenuation curve. The intrinsic SED for each galaxy is constructed by assuming a simple stellar population with the same SFR( $H\alpha$ ) and  $M^*$  as measured for that galaxy. The individual SEDs of objects in each bin of sSFR and  $\tau_b$  are then averaged together to produce the curves shown in the figure. The bottom panel shows the implied correction factors to the selective attenuation curves due to differences in the intrinsic SEDs of galaxies from bin-to-bin. Right: comparison of the  $fQ_{\text{eff}}$  (thin lines) with the versions corrected for variations in the intrinsic SEDs (thick lines) for each bin of sSFR.

derived above:  $\Delta Q_{\text{int}} \equiv 1./(\tau_i - \tau_1) \times \ln(f_i^{\text{int}}/f_1^{\text{int}})$ , where  $f_i^{\text{int}}$  is the intrinsic spectrum inferred for the  $i^{\text{th}}$  bin of  $\tau_b$ . These correction factors, as a function of wavelength, are also shown in the bottom of the left panel of Figure 11.

Third, we computed the corrected  $Q_i$  as  $Q_i^{\text{cor}} = Q_i + \Delta Q_{\text{int}}$ . We then followed the same procedure discussed above to compute  $fQ_{\text{eff}}^{\text{cor}}$ : the  $Q_i^{\text{cor}}$  in each bin of sSFR were averaged together to produce  $Q_{\text{eff}}^{\text{cor}}$  for each sSFR bin, third-order polynomials were fit to  $Q_{\text{eff}}^{\text{cor}}$ , and these functions were multiplied by the relevant correction factors according to Equation (6). Figure 11 indicates that the  $fQ_{\text{eff}}^{\text{cor}}$  are essentially identical to the uncorrected versions initially shown in Figure 9. In effect, correcting for the small differences in the intrinsic SEDs is mostly compensated for by the multiplicative factors  $f$ , which are smaller for the corrected  $Q_i$ . The ratios of the uncorrected to corrected  $fQ_{\text{eff}}$  at  $\lambda = 0.15$  and  $2.20 \mu\text{m}$  are 1.083 and 0.998, respectively, for sSFR bin 1; and 0.992 and 1.056, respectively, for sSFR bin 2. Given the less than  $\approx 8\%$  differences implied for the total attenuation curve, we assume the uncorrected version expressed in Equation (8).

Finally, we note that systematic offsets in the derived stellar masses or SFR( $H\alpha$ ) resulting from the assumption of different attenuation curves in the SED fitting will simply shift all the galaxies up or down in terms of sSFR, but the *ordering* of the galaxies will for the most part be preserved.<sup>11</sup> For this reason, the ratios of the intrinsic SEDs shown in Figure 11 will be unaffected by assuming a different attenuation curve in the derivation of SFR( $H\alpha$ ) and  $M^*$ . Detailed comparisons of the SED parameters and SFRs derived with different assumptions of the attenuation curve are presented in Section 4.

### 3.6.5. Comparison to Other Common Curves

The average attenuation curve found for the MOSDEF galaxies is compared to several local line-of-sight extinction curves and the Calzetti et al. (2000) attenuation curve in

<sup>11</sup> The ordering of galaxies will be preserved if the same attenuation curve applies to all galaxies. This is the case for galaxies in our sample, given the similarity in shape between  $Q_2$  and  $Q_3$  in a given sSFR bin (Figure 8), and the similarity in shape of  $fQ_{\text{eff}}$  between the two sSFR bins (Figure 9).

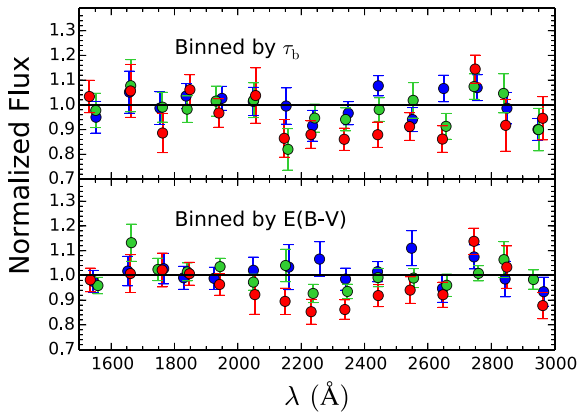


**Figure 12.** Normalized average photometry as a function of rest-frame wavelength for galaxies in bins of Balmer optical depth (top) and color excess of the stellar continuum (bottom). The average photometry of galaxies is computed in bins of rest-frame wavelength of  $\Delta\lambda = 100 \text{ \AA}$ , and the average photometry is normalized using a linear fit to the points over wavelength ranges  $\lambda = 1500\text{--}1800$  and  $2600\text{--}3000 \text{ \AA}$ .

Figure 10. The SMC, LMC, and Milky Way curves, and their respective normalizations, are taken from Gordon et al. (2003). A common feature of these curves is that they all asymptote to zero as the dust absorption cross-section becomes negligible at long wavelengths, with a corresponding rapid rise in the attenuation curve toward shorter (UV) wavelengths. The one distinguishing feature of the Milky Way and LMC extinction curves, namely the  $2175 \text{ \AA}$  “bump” (Stecher & Donn 1965; Fitzpatrick & Massa 1986), is absent from the attenuation curve found for local UV starburst galaxies (Calzetti et al. 2000), but its presence to varying degrees has been noted in higher-redshift galaxies (e.g., Noll et al. 2009; Buat et al. 2011, 2012; Kriek & Conroy 2013; Scoville et al. 2015).

To ascertain the existence of this excess absorption, we examined the average photometry of galaxies in bins of  $\tau_b$  and  $E(B - V)$ , where the latter were determined from the SED modeling discussed in Section 2.6. To improve the rest-frame wavelength sampling of the average photometry, we include all galaxies irrespective of their sSFRs. We then calculated the average, and error in the average, flux densities in rest-frame wavelength bins of  $100 \text{ \AA}$  (e.g., similar to the method used previously to compare the average photometry of galaxies in our sample to the functional fit to the photometry; Figure 7). A linear function was fit to the log of the average flux density as a function of  $\log(\lambda)$  in two wavelength ranges bracketing the  $2175 \text{ \AA}$  feature:  $\lambda = 1500\text{--}1800$  and  $2600\text{--}3000 \text{ \AA}$ . The errors in the mean flux densities were used to weight the points in the fitting. The average flux densities throughout the wavelength range from 1500 to  $3000 \text{ \AA}$  were then divided by this linear function to produce the normalized points shown in Figure 12.

There is on average a lower flux at the wavelengths corresponding to roughly where the excess absorption would be expected.<sup>12</sup> While the depth of the absorption appears to be insensitive to  $\tau_b$ , there is still some marginal significance for a trend between the absorption depth and the color excess of the

<sup>12</sup> As the wavelength windows used to compute the UV slope largely exclude the region where we observe a deficit in the average normalized flux, the effect of imposing a linear fit to the flux as a function of wavelength will result in a minimal bias of  $\Delta\beta \lesssim 0.1$ . This small bias does not affect our conclusions regarding the contribution of A stars to the near-UV continuum (Section 3.3.2), although of course fitting the slope without the photometry that may be affected by the  $2175 \text{ \AA}$  absorption will result in larger random uncertainties.

stellar continuum. A Spearman correlation test implies that that the null hypothesis of no correlation between the depth of the  $2175 \text{ \AA}$  and the color excess of the stellar continuum can be ruled out at the  $\approx 3\sigma$  level. We caution that the excess absorption will be smoothed by the finite wavelength sampling of the average photometry, as well as the fact that the average photometry is computed from broad- and intermediate-band magnitudes.

For comparison, Buat et al. (2012) deduce the shape of the dust attenuation curve for a sample of 751 galaxies at  $0.95 < z < 2.2$ , and find evidence for excess absorption at  $2175 \text{ \AA}$  for roughly 20% of their sample, almost all (90%) of which lie at  $z < 1.5$ . They also find that the rate of a secure detection of bump increases by a factor of  $\approx 2$  when considering the dustier galaxies (i.e., those directly detected at mid- and far-IR wavelengths). In another recent study, Kriek & Conroy (2013) examine a sample of somewhat lower-redshift ( $0.5 < z < 2.0$ ) galaxies and find that the strength of the  $2175 \text{ \AA}$  absorption correlates with the “steepness” (i.e., the wavelength dependence) of the attenuation curve. However, we note that the galaxies in their sample have  $W_{H\alpha} < 140 \text{ \AA}$ , values that are substantially lower (corresponding to lower sSFRs) than those considered here ( $W_{H\alpha} \gtrsim 100 \text{ \AA}$ ). More definitive results on the extent to which the  $2175 \text{ \AA}$  absorption may be present in the galaxies targeted with MOSDEF, as well as the characteristics (e.g., slope of the attenuation curve, sSFR, redshift) upon which its depth may depend, will come from the larger (completed) survey dataset.

Regardless, our analysis shows that the attenuation curve for the MOSDEF galaxies exhibits a slope that is identical to that of the Calzetti et al. (2000) attenuation curve for  $\lambda < 0.6 \mu\text{m}$ , but with a lower normalization ( $R_V$ ). For  $\lambda > 0.6 \mu\text{m}$ , the MOSDEF curve is similar to that of the SMC curve, and more generally, the two are essentially identical for  $\lambda > 0.25 \mu\text{m}$ . Recent studies have suggested that some populations of high-redshift galaxies have reddening that is consistent with the SMC (e.g., Reddy et al. 2006, 2010; Siana et al. 2008, 2009; Shim et al. 2011; Oesch et al. 2013). Here, we have shown that through direct measurements of the attenuation curve, an SMC-like behavior at longer wavelengths ( $\lambda > 2500 \text{ \AA}$ ) may be more generally applicable at high redshift. A comparison between the physical models of the distribution of dust and stars in galaxies and the attenuation curve will be presented elsewhere, but we note that the shape of the attenuation curve may imply a larger covering fraction of dust in the rest-optical, or a different dust grain size distribution, than would be indicated by the Calzetti et al. (2000) curve. The implications for these differences in the shapes of the attenuation curves are discussed in the next section.

## 4. DISCUSSION AND IMPLICATIONS

### 4.1. Reassessment of the Stellar Populations

Given the apparent differences in the attenuation curve derived in this work relative to the curve typically assumed for high-redshift galaxies (i.e., Calzetti et al. 2000), we adopted our new calculation of the attenuation curve to refit the stellar populations of galaxies in our sample, in the same way as described in Section 2.6. The comparison of several stellar population parameters using our new curve versus those obtained with the Calzetti et al. (2000) and SMC curves is shown in Figure 13. The mean color excess of the stellar continuum assuming the MOSDEF attenuation curve is  $\langle \Delta E(B - V) \rangle \approx 0.02$  redder than that obtained with the Calzetti et al. (2000) relation ( $E(B - V) \approx 0.19$  versus

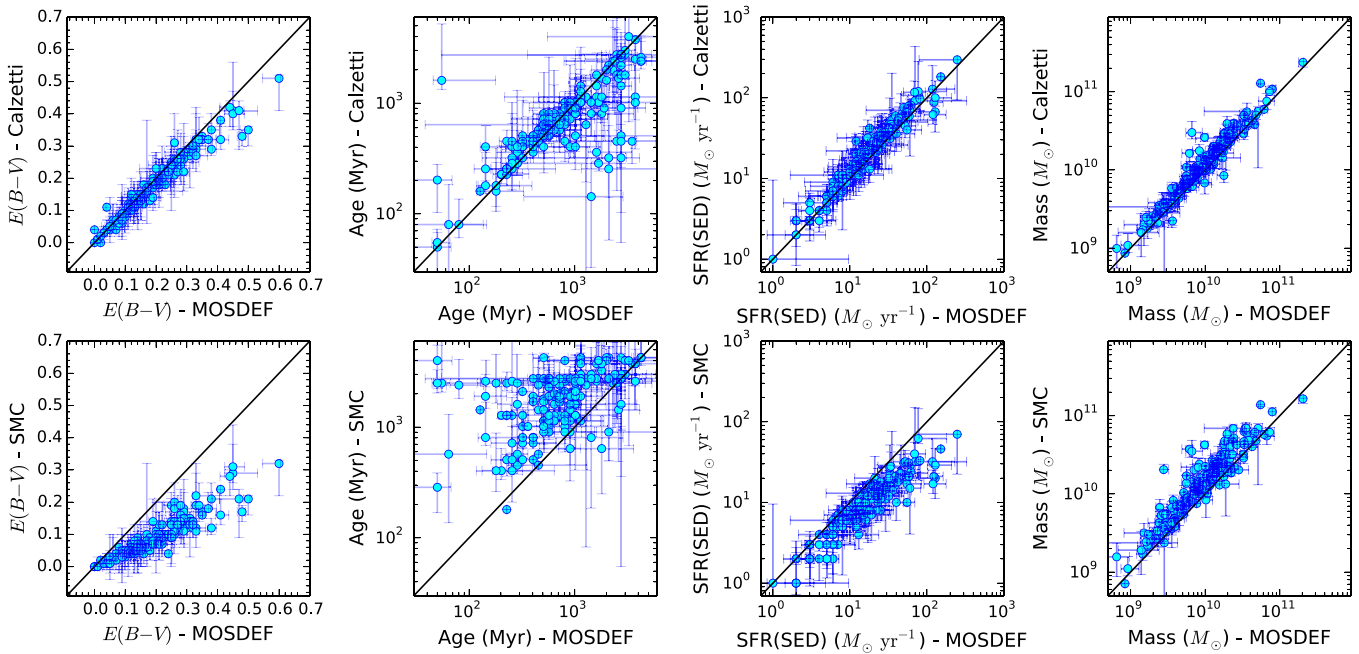


**Figure 13.** Comparison of the color excesses, ages, SFRs, and stellar masses returned from SED fitting assuming our new attenuation curve relative to those obtained with the Calzetti et al. (2000) and SMC attenuation curves. The solid lines denote a one-to-one agreement between the plotted quantities.

0.17). Combining this average difference in the color excesses with the  $\Delta k \approx 1.63$  difference in the two attenuation curves at  $\lambda = 1600 \text{ \AA}$ , we infer dust obscuration factors (required to deredden the observed UV SFRs) that are  $10^{0.09} \approx 1.2$  times smaller than those inferred from the Calzetti et al. (2000) relation. As a result, the average SED-inferred SFRs obtained with the MOSDEF attenuation curve are  $\approx 20\%$  smaller than those obtained with a Calzetti et al. (2000) curve. This systematic difference in the SFRs is typically smaller than the random uncertainties, where the latter were computed using Monte Carlo realizations of the observed photometry and refitting the model SEDs to the perturbed photometry; Section 2.6). Similarly, the systematic offset seen here is well within the typical factor of  $\approx 2$  uncertainty in independent measurements of the SFRs based on combining UV and IR data for galaxies with similar SFRs and stellar masses, and at the same redshifts, as those considered here (Reddy et al. 2006, 2010, 2012a; Daddi et al. 2007). These results apply on average, as it is clear from Figure 13 that the difference in  $E(B - V)$  implied by the two attenuation curves is a function of the “redness” of the object. For the bluest galaxies, we find  $\Delta E(B - V) \approx 0$  (these are galaxies for which little reddening is required to reproduce the UV colors). For the reddest galaxies (e.g., those with  $E(B - V) > 0.3$  as computed from the MOSDEF attenuation curve), we find  $\Delta E(B - V) \approx 0.08$ .

Assuming the MOSDEF attenuation curve results in galaxies that are on average  $\approx 300$  Myr older relative to the ages derived using the Calzetti et al. (2000) curve, however we view these differences to be negligible given the large uncertainties in the ages.<sup>13</sup> Note that the “uncertainties” quoted here do not account

<sup>13</sup> A subset of objects have “best-fit” ages that are a factor of  $\geq 2$  older with the MOSDEF attenuation curve relative to those obtained with the Calzetti et al. (2000) curve. These are objects where the MOSDEF and Calzetti et al. (2000) “best-fit” SEDs are essentially identical in the rest-frame optical, but where the former are generally fainter in the rest-frame near-IR. As such, the implied Balmer/4000  $\text{\AA}$  breaks are stronger for the MOSDEF “best-fit” SEDs resulting in older ages.

for other systematic effects, including differences in the assumed star formation histories of galaxies. Finally, we note that assuming the MOSDEF attenuation curve yields better fits to the longer wavelength (i.e., rest-frame  $\approx 1.0\text{--}2.5 \mu\text{m}$ ) photometry than the Calzetti et al. (2000) curve for rising star formation histories (Figure 14). As such, the stellar masses are  $\approx 25\%$  lower when we adopt the MOSDEF attenuation curve in lieu of the Calzetti et al. (2000) curve. This implies an  $\approx 0.1$  dex difference in  $\log M^*$  that is of the same order as the uncertainty in the stellar mass implied by the photometric errors. Similarly, in comparison to the results derived with an SMC attenuation curve, those assuming the MOSDEF curve imply significantly redder  $E(B - V)$  ( $\Delta E(B - V) \approx 0.10$ ), younger ages (by a factor of  $\approx 2$ ), higher SFRs (by a factor of  $\approx 2$ ), and lower stellar masses ( $\Delta \log(M^*/M_\odot) \approx 0.16$  dex). The differences stem from the fact that the SMC curve has a steeper wavelength dependence in the UV than either the MOSDEF or Calzetti et al. (2000) attenuation curves, and thus a lower amount of reddening is required to fit a given UV-color. As a result, the SFRs are lower with the SMC curve. Further, the near-IR-optical color is attributed more to an older stellar population than dust reddening, resulting in older ages and larger stellar masses.

Another point of consideration is how the sSFRs are affected by different assumptions of the attenuation curve. Recall that the sSFRs were calculated by combining  $H\alpha$ -based SFRs, which were determined independently of SED fitting, with the SED-based stellar masses (Section 2.6). The  $H\alpha$ -based SFRs were derived assuming the Cardelli et al. (1989) extinction curve (Section 2.8). The SED-based stellar masses were computed assuming the Calzetti et al. (2000) curve. We will return to a more detailed discussion of the implications of our results for SFR determinations (Section 4.4), but for the remainder of our analysis, we adopt the sSFRs computed assuming the stellar masses obtained with the MOSDEF attenuation curve, and SFR( $H\alpha$ ) obtained with the Cardelli

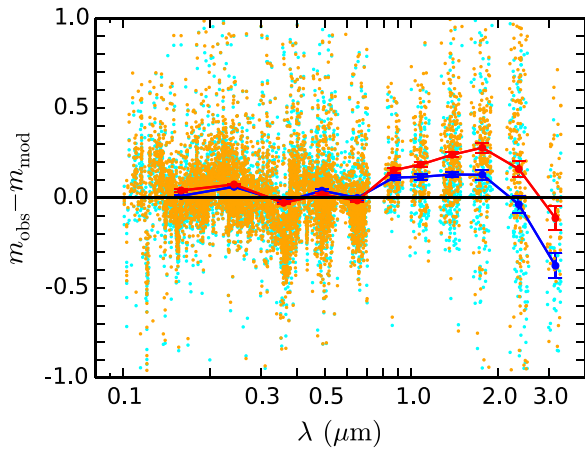


**Figure 14.** Residuals (i.e., difference in the observed and model photometry) for galaxies in our sample assuming a rising star formation history and the MOSDEF (cyan) and Calzetti et al. (2000) (orange) attenuation curves. The mean residuals and the errors in these means are indicated by the blue and red symbols, assuming the MOSDEF and Calzetti et al. (2000) curves, respectively. For rest-frame wavelengths between  $\approx 1$  and  $2.5 \mu\text{m}$ , the MOSDEF attenuation curve results in a statistically significant improved fit to the observed photometry, on average, relative to that obtained assuming the Calzetti et al. (2000) curve.

et al. (1989) extinction curve. As shown in Figure 15, the new sSFRs computed in this way are quite similar to those computed when we assume the Calzetti et al. (2000) attenuation curve in deriving the stellar masses, with the former being  $\Delta \log(\text{sSFR}/\text{yr}^{-1}) \simeq 0.09$  dex smaller than the latter. Because there is only a systematic offset between the two sSFR determinations, and the relative ordering of the galaxies is preserved, the sSFR bins used to calculate the attenuation curve (Section 3.6.1) will include essentially the same set of galaxies regardless of which attenuation curve is assumed (and, in any case, the results of Section 3.6.1 suggest that because the attenuation curves computed from the two sSFR bins are very similar, we could have simply ignored any binning with sSFR in computing the curve).

#### 4.2. Measurements of UV Slopes

As noted in Section 3.3.2,  $\beta_{\text{phot}}(1260\text{--}1750 \text{ \AA})$  is not substantially bluer than  $\beta_{\text{phot}}(1260\text{--}2600 \text{ \AA})$ , suggesting that A stars do not contribute significantly to the UV continuum for the galaxies in our sample. It is worthwhile to consider this point further, because an intrinsically blue spectral slope in the range  $1260\text{--}1750 \text{ \AA}$  can appear redder than the slope measured over the wider baseline in wavelength ( $1260\text{--}2600 \text{ \AA}$ ) if the attenuation curve is rising steeply in the UV. Therefore, we must rule out the case where the attenuation curve masks the contribution from A stars to the near-UV continuum. Our new derivation of the attenuation curve implies that the difference between  $\beta(1260\text{--}1750 \text{ \AA})$  and  $\beta(1260\text{--}2600 \text{ \AA})$  for galaxies where the latter is  $< 0.5$  (a limit that encompasses almost all of the galaxies in our sample), is  $\Delta\beta < 0.2$  for  $E(B - V) \lesssim 0.4$ . This difference in UV slope is small compared to both the typical measurement errors in the UV slopes and the dispersion in  $\beta(1260\text{--}1750 \text{ \AA})$  at a given  $\beta(1260\text{--}2600 \text{ \AA})$  (Figure 4). Thus, the reddening implied by the MOSDEF attenuation curve is insufficient to make an intrinsically blue  $\beta(1260\text{--}1750 \text{ \AA})$  appear substantially redder than  $\beta(1260\text{--}2600 \text{ \AA})$ , and our

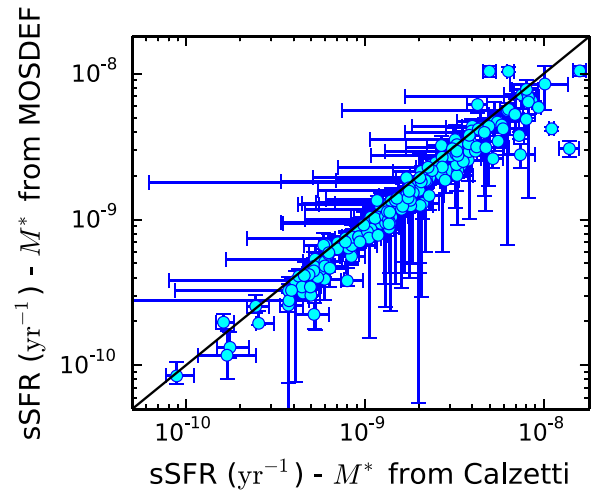


**Figure 15.** Specific SFRs calculated assuming  $\text{H}\alpha$ -based SFRs, and stellar masses from SED fitting. SFR( $\text{H}\alpha$ ) assumes the Cardelli et al. (1989) extinction curve. The stellar masses assume the Calzetti et al. (2000) (ordinate) and the MOSDEF (abscissa) attenuation curves.

conclusion regarding the contribution of A stars to the UV continuum still holds.

The test just discussed allows us to calculate the useful relationship between  $\beta$  and the color excess of the stellar continuum assuming the MOSDEF attenuation curve and an underlying solar metallicity stellar population with constant star formation for at least 100 Myr (i.e., with an intrinsic spectral slope of  $\beta_{\text{int}} \approx -2.44$ ):  $\beta = -2.44 + 4.54 \times E(B - V)$ . Additionally, Equations (5) and (8) imply that the attenuation in magnitudes at  $1600 \text{ \AA}$  is related to the color excess by  $A_{1600\text{\AA}} = 8.34 \times E(B - V)$ . Thus, combining the previous two equations, we find

$$A_{1600\text{\AA}} = 1.84\beta + 4.48, \quad (9)$$

again for an intrinsic spectral slope  $\beta_{\text{int}} \simeq -2.44$ . For comparison, the relation from Meurer et al. (1999) is  $A_{1600\text{\AA}} = 1.99\beta + 4.43$ , or  $A_{1600\text{\AA}} = 1.99\beta + 4.86$  when shifted to account for the difference in the intrinsic UV slope ( $\beta_0$ ) between Meurer et al. (1999) and the present study (i.e.,  $\beta_0 = -2.23$  versus  $-2.44$ ). Consequently, for the bulk of the galaxies in our sample with  $\beta < -0.5$ , the implied difference in the magnitudes of extinction at  $1600 \text{ \AA}$ , when assuming the MOSDEF and Meurer et al. (1999) attenuation curves, is  $\Delta A_{1600\text{\AA}} \lesssim 0.31$ . More specifically, the MOSDEF attenuation curve implies dust obscuration factors,  $10^{[0.4 \times A(1600\text{\AA})]}$ , that are a factor of  $\lesssim 1.32$  times lower than those implied by the Meurer et al. (1999; or Calzetti et al. 2000) attenuation curve, with an average correction that results in SFRs that are  $\approx 20\%$  lower for the MOSDEF curve, as noted above. Equation (9) can be used to directly determine the attenuation of the UV continuum for galaxies of a given (measured) UV slope. However, as we discuss in Section 4.4, additional factors may be required to recover total SFRs from UV-based ones.

#### 4.3. Comparison of the Color Excesses and Total Attenuation of the Stellar Continuum and Ionized Gas

There has been a considerable effort to investigate the relationship between the attenuation of the stellar continuum

and ionized gas in high-redshift galaxies, particularly in light of local observations of star-forming galaxies (e.g., Fanelli et al. 1988; Calzetti et al. 1994; Mas-Hesse & Kunth 1999; Moustakas & Kennicutt 2006; Kreckel et al. 2013), which suggest a higher reddening of the ionized gas than of the stellar continuum (e.g.,  $E(B - V)_{\text{stars}} = 0.44 \times E(B - V)_{\text{gas}}$ ; Calzetti et al. 2000). Note that this often-quoted relationship describes the color excess of the stellar continuum and the nebular line-emitting regions, not the total attenuation. More precisely, this relation is derived under the assumption that the starburst attenuation curve applies to the stellar continuum, and a Galactic extinction curve (Cardelli et al. 1989) applies to the ionized gas (Calzetti 2001). However, most investigations of the stellar and nebular reddening in high-redshift galaxies have assumed that the same attenuation curve applies for both the gas and the stars, and it is unclear if this is an appropriate assumption in the context of high-redshift galaxies.

From the standpoint of local galaxies, the difference in attenuation curves can be understood in the framework where the recombination emission arises from spatially compact H II regions that are subject to a high covering fraction of dust and where a line-of-sight extinction curve (e.g., Cardelli et al. 1989 or SMC) is more appropriate, versus the more spatially extended stellar continuum that has a lower dust-covering fraction and is subject to a “grayer” attenuation curve (e.g., Calzetti et al. 2000). This configuration is similar to the two component dust model of Charlot & Fall (2000), where the H II regions are attenuated by a component of dust in undissipated parent birth clouds, with a second diffuse component of dust in the ISM.

Studies of UV-selected galaxies at  $z \sim 2$  have shown a general agreement between UV and H $\alpha$ -based SFRs when applying the same color excess and assuming that the same attenuation curve applies for both the stars and gas (e.g., Erb et al. 2006a; Reddy et al. 2010; Shivaei et al. 2015; see also Cowie & Barger 2008 for results at  $z < 0.5$ ). On the other hand, studies that have targeted on average more highly star-forming or more massive galaxies, and/or photometrically selected galaxies, indicate a higher attenuation of the gas versus the stellar continuum, again with most studies assuming that the same attenuation curve applies for both the stars and gas (e.g., Förster Schreiber et al. 2009; Yoshikawa et al. 2010; Wuyts et al. 2011; Kashino et al. 2013; Wuyts et al. 2013; Price et al. 2014).

#### 4.3.1. Comparison of Color Excesses

A plausible scenario that can resolve the current observations is one in which the difference in the continuum and nebular attenuation is a function of SFR, mass, or sSFR (e.g., Reddy et al. 2010; Price et al. 2014). As noted in Section 3.6.2, the selective attenuation curve derived in this study implies that *on average* the ionized gas suffers greater extinction than the continuum (at the wavelengths of H $\alpha$  and H $\beta$ ). We scrutinized this result by comparing the color excesses of the stellar continuum derived from SED fitting with those of the ionized gas, computed as:

$$\begin{aligned} E(B - V)_{\text{gas}} &= \frac{2.5}{k(\text{H}\beta) - k(\text{H}\alpha)} \log_{10} \left( \frac{\text{H}\alpha/\text{H}\beta}{2.86} \right) \\ &= \frac{1.086}{k(\text{H}\beta) - k(\text{H}\alpha)} \tau_b \simeq 0.950 \tau_b. \end{aligned} \quad (10)$$

In the last step, we assumed that the Cardelli et al. (1989) extinction curve applies to the H II regions. Adopting the Calzetti et al. (2000) and MOSDEF attenuation curves results in  $E(B - V)_{\text{gas}}$  values that are a factor of 0.90 $\times$  and 1.01 $\times$  those assuming the Cardelli et al. (1989) curve, respectively. There is a large scatter in the relationship between the gas and continuum color excesses, with  $\approx 50\%$  of the objects having equal gas and continuum color excesses within the ( $1\sigma$ ) uncertainties, and only 7% consistent with having  $E(B - V)_{\text{gas}} > E(B - V)_{\text{stars}}/0.44$ . As could have been anticipated from Figures 2 and 3, the degree to which  $E(B - V)_{\text{gas}}$  diverges from  $E(B - V)_{\text{stars}}$  is dependent upon the sSFR of the galaxy, with the largest differences for galaxies with the largest sSFRs (Figure 16).<sup>14</sup>

We should consider, however, whether selection biases could result in a correlation between the difference in the gas and nebular color excesses and the sSFR. In particular, if galaxies with H $\alpha$  fluxes close to our detection limit of  $\simeq 5 \times 10^{-18} \text{ erg s}^{-1} \text{ cm}^{-2}$  are dusty, then their H $\beta$  lines may be undetected with a greater frequency than galaxies of the same dust content but with bright H $\alpha$  lines. As a result, we may be insensitive to galaxies with low SFRs and high nebular color excesses. However, as seen in Figure 1, the H $\beta$ -undetected galaxies in our sample have limits that span the full range of observed  $L_{\text{H}\alpha}$ . Further, if we compute the average SFR(H $\alpha$ ), sSFR,  $E(B - V)_{\text{gas}}$ , and  $E(B - V)_{\text{stars}}$  for the H $\beta$ -undetected galaxies, as shown in Figures 16 and 17 (where the averages for the SFR and  $E(B - V)_{\text{gas}}$  are determined from the composite stack of their spectra; Section 2), the aforementioned quantities suggest that there is not a large population of dusty galaxies with low SFRs and low sSFRs. Aside from this direct observation, it has been shown in several studies that the mean obscuration of high-redshift galaxies increases with SFR (e.g., Adelberger & Steidel 2000; Reddy et al. 2006, 2008, 2010; Buat et al. 2007, 2009; Burgarella et al. 2009; Sobral et al. 2012; Domínguez et al. 2013; see also discussion below), suggesting that among galaxies with low H $\alpha$  fluxes, those that are intrinsically less dusty vastly outnumber those with high dust content. The stacking of mid- to far-IR data for the MOSDEF galaxies will help to clarify these arguments. There is no similar bias in terms of  $E(B - V)_{\text{stars}}$ , as the spectroscopically confirmed MOSDEF galaxies have rest-UV colors similar to those of galaxies in the parent sample (Kriek et al. 2015).

Formally, a Kendall’s  $\tau$  test indicates a probability of  $\lesssim 1.8 \times 10^{-7}$  that the difference between gas and stellar color excesses is *uncorrelated* with sSFR. The correlation with H $\alpha$ -based SFR is even stronger, with  $\lesssim 10^{-9}$  probability that  $E(B - V)_{\text{gas}} - E(B - V)_{\text{stars}}$  is uncorrelated with SFR (Figure 17). Similarly, there is a  $\lesssim 10^{-4}$  probability that the difference in color excesses is uncorrelated with stellar mass. Thus, the conflicting results on the relationship between the color excesses of the H II regions and stellar continuum in high-redshift galaxies can be reconciled if selection over different ranges of SFR and/or stellar mass leads to the inclusion of more or fewer galaxies with the largest discrepancies between nebular and continuum color excess. Specifically, galaxies with

<sup>14</sup> As shown in Section 4.4.2, a *different* relation is found between  $E(B - V)_{\text{gas}} - E(B - V)_{\text{stars}}$  and sSFR(SED) (i.e., the sSFR computed when we use *SED-based* SFRs).

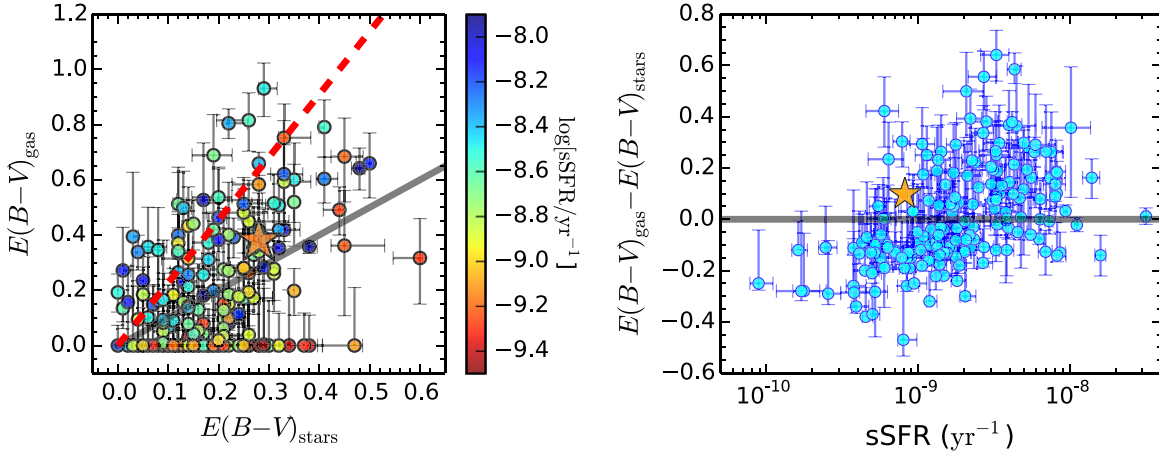


**Figure 16.** Left: comparison of the color excesses derived for the stellar continuum and the ionized gas.  $E(B - V)_{\text{gas}}$  is computed assuming the Cardelli et al. (1989) extinction curve, and  $E(B - V)_{\text{stars}}$  is the value returned from the SED fitting when we assume the MOSDEF attenuation curve. The solid line denotes identical color excesses derived for the stellar and gas components, and the dashed line indicates the relation  $E(B - V)_{\text{gas}} = E(B - V)_{\text{stars}}/0.44$  from Calzetti et al. (2000). Points are differentiated according to the sSFR. The large star denotes the average values for the  $H\beta$ -undetected galaxies. Right: the difference between the gas and continuum color excesses as a function of sSFR, where the solid line indicates no difference between the color excess of the nebular regions and the stellar continuum. The large star denotes the average values for the  $H\beta$ -undetected galaxies.

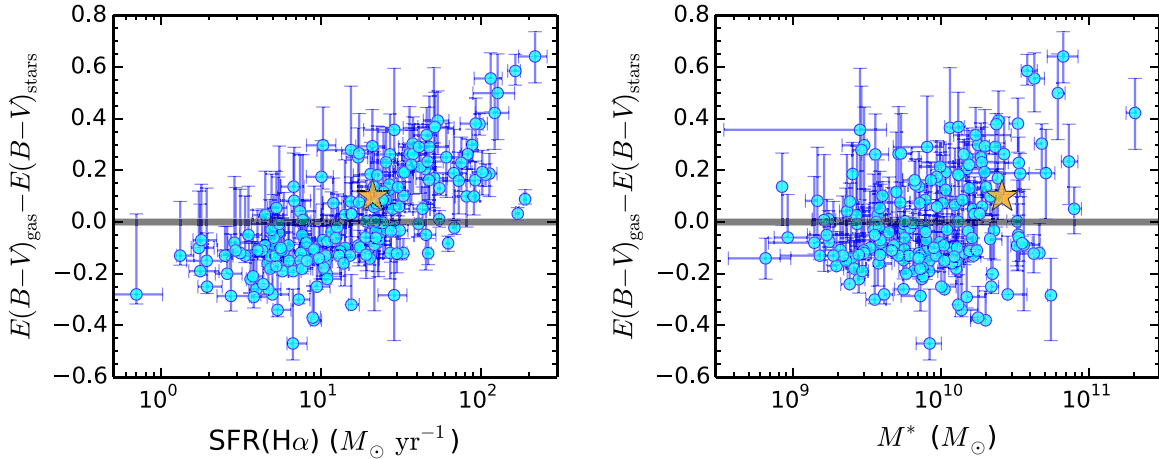


**Figure 17.** Difference between gas and continuum color excesses as a function of  $H\alpha$  SFR (left) and stellar mass (right), where the solid lines indicate no difference between the color excess of the nebular regions and the stellar continuum, and the large stars indicate the values for  $H\beta$ -undetected galaxies.  $SFR(H\alpha)$  is computed assuming the Cardelli et al. (1989) extinction curve.

$SFRs \gtrsim 20 M_{\odot} \text{ yr}^{-1}$  exhibit nebular color excesses that are substantially redder than the continuum color excesses.

In contrast, over the range of SFRs characteristic of UV-selected galaxies at  $z \sim 2$  ( $\lesssim 20 M_{\odot} \text{ yr}^{-1}$  for a Chabrier IMF; e.g., Reddy et al. 2012b), the nebular color excesses are essentially equivalent to or bluer than those of the stellar continuum. Of the 51 objects that have an  $E(B - V)_{\text{gas}}$  that is more than  $1\sigma$  bluer than  $E(B - V)_{\text{stars}}$ , 35 (or  $\approx 69\%$ ) formally have  $E(B - V)_{\text{gas}} = 0$ . These galaxies are unlikely to have  $H\text{II}$  regions that are completely dust-free given the reasoning presented in Section 3.5, and their  $E(B - V)_{\text{stars}}$  span the full range observed for galaxies in our sample in general. An analysis of the spatially resolved colors of these galaxies should lend more insight into the question of why they exhibit  $E(B - V)_{\text{gas}}$  that is bluer than the color excess of the stellar continuum. In summary, we find that the difference in the color

excesses of the stellar continuum and ionized gas in high-redshift galaxies is a strong function of SFR: above an SFR of  $\approx 20 M_{\odot} \text{ yr}^{-1}$ , the nebular lines become increasingly reddened relative to the color excess of the stellar continuum.

#### 4.3.2. Comparison of the Total Attenuation of the Ionized Gas and Stellar Continuum

So far, our discussion has focused on a comparison of the color excesses of the ionized gas and the stellar continuum in high-redshift galaxies. Recall that the color excess of the ionized gas was computed assuming the Cardelli et al. (1989) extinction curve. The color excess of the stellar continuum was derived assuming the MOSDEF attenuation curve. These respective curves were also used to compute the total attenuation in magnitudes of the line and continuum emission

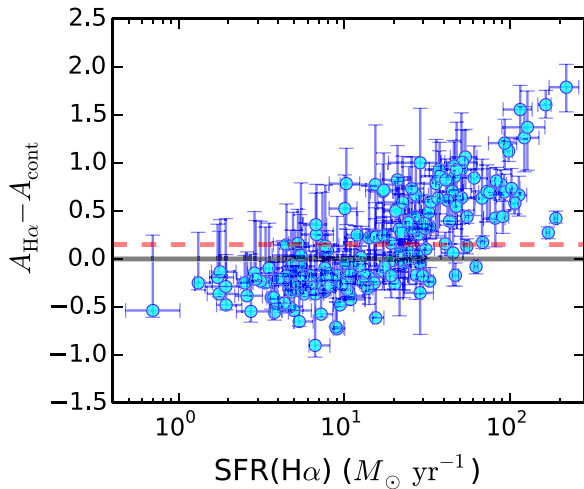


**Figure 18.** Difference between the magnitudes of attenuation of recombination line photons and continuum photons at 6565 Å, as a function of SFR.  $A_{H\alpha}$  and  $A_{\text{cont}}$  assume the Cardelli et al. (1989) Galactic extinction curve and the MOSDEF attenuation curve, respectively. The solid and dashed lines denote equal attenuation and the mean difference ( $\langle A_{H\alpha} - A_{\text{cont}} \rangle \simeq 0.15$ ) in attenuation of line and continuum photons, respectively.

at 6565 Å:

$$\begin{aligned}
 A_{H\alpha} &= k_{\text{Cardelli}}(6565 \text{ \AA}) \times E(B - V)_{\text{gas}} \\
 &= 2.52 \times E(B - V)_{\text{gas}}; \\
 A_{\text{cont}} &= k_{\text{MOSDEF}}(6565 \text{ \AA}) \times E(B - V)_{\text{stars}} \\
 &= 1.92 \times E(B - V)_{\text{stars}}.
 \end{aligned} \tag{11}$$

The comparison of  $A_{H\alpha}$  and  $A_{\text{cont}}$  (Figure 18) confirms the result noted in Section 3.6.2, namely that the ionized gas is on average more obscured than the stellar continuum. Specifically, we find that the average difference in the magnitudes of attenuation between the recombination line and continuum photons at 6565 Å is  $\langle A_{H\alpha} - A_{\text{cont}} \rangle \simeq 0.15$ . However, as was the case in the comparison of the color excesses, we find that the difference in the total attenuation of line and continuum photons depends on the SFR, such that galaxies with the largest SFRs can exhibit line-emitting regions that are half a magnitude (or more) attenuated than the stellar continuum.

#### 4.3.3. Physical Interpretation

A final point of consideration is the strong dependence of total dust attenuation on SFR (Figure 19). Such a correlation has been noted before both at low (Wang & Heckman 1996; Hopkins et al. 2001) and high redshift (e.g., Adelberger & Steidel 2000; Reddy et al. 2006, 2008, 2010; Buat et al. 2007, 2009; Burgarella et al. 2009; Sobral et al. 2012; Domínguez et al. 2013), and has also been shown to evolve with redshift (e.g., Reddy et al. 2010; Domínguez et al. 2013). Physically, this trend can be understood as the product of increased metal and dust enrichment of the ISM with increasing SFR. In the context of the present study, a *possible* simple model that can account for the trends in ionized gas versus continuum attenuation is one in which a modestly reddened stellar population dominates the observed UV through optical continuum emission of galaxies over the entire range of SFRs considered here. Meanwhile, as the total SFR rises, a greater fraction of this SFR is obscured in optically thick regions, as a

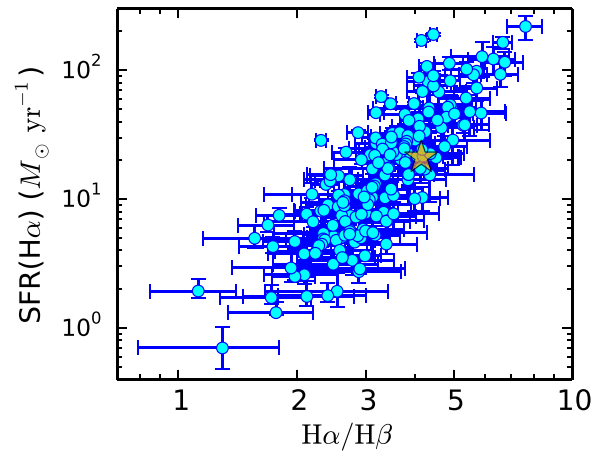


**Figure 19.**  $H\alpha$ -based SFR vs. Balmer decrement. The large star denotes the average values for the  $H\beta$ -undetected galaxies. Note that the Balmer decrement is used in the calculation of the SFR, resulting in a tightening of the scatter shown here. Nonetheless, the results suggest the same trend between SFR and dustiness that has been noted in other studies at low and high redshift (see text).

consequence of the increased dust enrichment that accompanies galaxies with larger SFRs. As a result, the *average* optical depth toward ionizing stars rises with SFR. This simple picture is illustrated in Figure 20. We emphasize that this is an “average” effect, as it is clear that some fraction of O stars are in relatively unobscured regions of the galaxies where they can contribute significantly to the UV continuum and where the average reddening (as measured by the UV slope,  $\beta$ ) is lower than that measured from the Balmer lines.

The framework just discussed is somewhat different than the one originally invoked to explain the disparity between the gas and continuum color excesses in the local Universe. Locally, such a discrepancy between color excesses is thought to arise from the increased dust-covering fraction surrounding H II regions (e.g., perhaps due to undissipated parent birth clouds surrounding the youngest stars; Calzetti et al. 1994). If this is the case at high redshift (i.e., that *most* of the short-lived O stars reside in or close to their parent molecular clouds), then we should see a *systematic* offset between gas and continuum color excesses at all SFRs. However, this expected systematic offset is not seen in our data (e.g., Figures 16–18). Rather, our results suggest two distinct stellar populations in each galaxy: one in which stars of all masses are subject to modest amounts of dust reddening and which dominate the observed UV through optical continuum luminosity; and another in which stars of all masses reside in very dusty regions. The second population becomes more dominant over the first population (in terms of its contribution to the nebular line and bolometric luminosities) as the total SFR of a galaxy increases. Consequently, the color excesses (and total attenuation) of the gas and continuum diverge with rising SFR. This simple picture may also imply that the attenuation curve relevant for the ionized gas may transition from a gray curve (e.g., Calzetti et al. 2000) to a progressively “steeper” (e.g., Galactic or SMC) curve with increasing SFR.

Along these lines, more recent high spatial resolution observations of several nearby galaxies suggest that the relationship between the attenuation of the gas and stars varies with SFR surface density ( $\Sigma_{\text{SFR}}$ ), such that the Balmer lines are

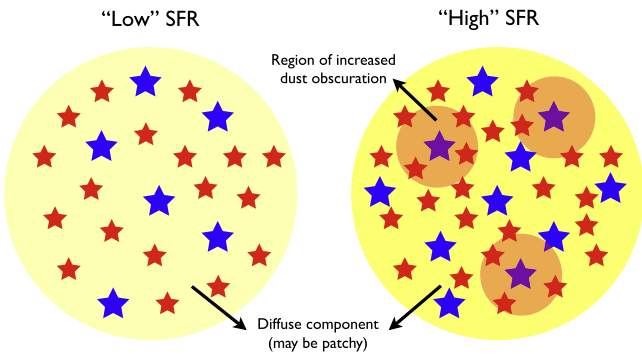


**Figure 20.** Illustration of a simple geometry of dust and gas that can account for the trends in the difference between ionized gas and continuum color excess, and total attenuation, vs. SFR. The yellow region denotes the diffuse dust component (which may be patchy). The red regions indicate areas of increased dustiness within the galaxy. The red and blue stars indicate high mass (ionizing) and lower mass stars, respectively. At lower SFRs ( $\lesssim 20 M_{\odot} \text{ yr}^{-1}$ ), stars of all masses are uniformly obscured. As the SFR increases, the diffuse component becomes more dust-enriched (as indicated by the darker shade of yellow), while regions of more highly obscured SFR (red regions) become prominent. As the SFR increases, these more obscured regions begin to dominate the nebular line and bolometric luminosities. The diffuse component dominates the UV through optical SED at both low and high SFRs.

systematically more attenuated than the stellar continuum for regions where  $\Sigma_{\text{SFR}} \gtrsim 0.01 M_{\odot} \text{ yr}^{-1} \text{ kpc}^{-2}$  (e.g., see Figure 4 of Kreckel et al. 2013; see also Boquien et al. 2015). These observations have been interpreted as evidence that the Balmer lines are dominated by dust-buried H II regions at high  $\Sigma_{\text{SFR}}$  (Kreckel et al. 2013). If the higher SFR galaxies in our sample also have higher  $\Sigma_{\text{SFR}}$ , then the situation inferred locally on small scales (e.g., 100–200 pc) may also apply at high redshift. This issue can be addressed with the larger MOSDEF sample, which will include galaxy size information.

Our analysis demonstrates that while the wavelength dependence of the dust obscuration appears to be independent of sSFR, the *total* obscuration of the ionized gas relative to that of the stellar continuum varies with SFR and sSFR. Specifically, galaxies with larger SFRs (and sSFRs) exhibit redder color excesses and larger total attenuations for the line emission relative to those for the continuum. These trends are responsible for the scatter seen between  $\beta$  and  $\tau_b$  (Figure 2). The physical picture discussed here implies that galaxies with larger SFRs may exhibit a higher dispersion in their spatially resolved colors as the dust obscuration becomes more patchy with the rise of a second (dustier) population. Alternatively, the increased dust-covering fraction expected for galaxies with larger SFRs may be reflective of a compact configuration of the star formation. Hence, future prospects for elaborating on this simple picture will include a detailed analysis of how the SFR surface density, and the spatially resolved UV colors of galaxies—whose measurement is aided with deep high-resolution *HST* imaging in the fields targeted with MOSDEF—correlate with globally measured color excesses of the ionized gas and the stellar continuum.

#### 4.4. Implications for SFR Measurements

##### 4.4.1. $H\alpha$ and UV-based SFRs

As mentioned in Section 4.1, the SED-based SFRs assuming a MOSDEF attenuation curve are on average lower (by  $\approx 20\%$ ) than those determined with the Calzetti et al. (2000) curve. The

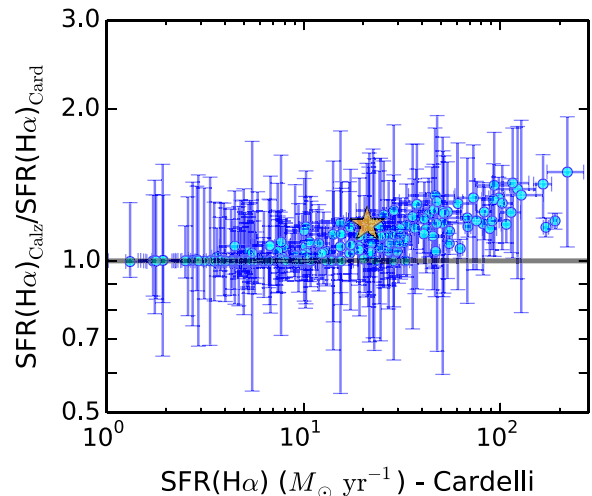


**Figure 21.** Ratio of  $H\alpha$ -based SFRs assuming the Calzetti et al. (2000) attenuation curve and the Cardelli et al. (1989) extinction curve, vs. the those assuming the Cardelli et al. (1989) extinction curve. The large star denotes the average values for the  $H\beta$ -undetected galaxies. Assuming that the Calzetti et al. (2000) attenuation curve applies to the H II regions of high-redshift galaxies results in dust-corrected  $\text{SFR}(H\alpha)$  that can be as much as  $\approx 50\%$  larger than those derived assuming the Cardelli et al. (1989) extinction curve.

$H\alpha$ -based SFRs also rely on an assumption of the attenuation curve, both in deriving the color excess of the ionized gas, and in applying the total dust correction to recover the intrinsic  $H\alpha$  SFRs. The default values of  $\text{SFR}(H\alpha)$  were computed assuming the Cardelli et al. (1989) extinction curve—that is, this curve was used to calculate  $E(B - V)_{\text{gas}}$  given the Balmer decrement, and the value of the curve at  $6565 \text{ \AA}$  was used to dust correct the observed  $H\alpha$  luminosity (Section 2.8). The more common practice of assuming that the Calzetti et al. (2000) curve applies to high-redshift H II regions results in SFRs that can be as much as  $\approx 50\%$  larger than those assuming the Cardelli et al. (1989) extinction curve (Figure 21), with an average offset of  $\approx 20\%$ . This comparison underscores the importance of considering the appropriate attenuation curve to use when dust correcting the line and continuum emission in high-redshift galaxies.

When compared against each other, the  $H\alpha$  and SED-determined SFRs show a general agreement, with a scatter of 0.34 dex (Figure 22). A similar agreement has been noted in Steidel et al. (2014), who also compare  $H\alpha$  and SED-based SFRs, but use a different prescription for estimating the color excess relevant for the nebular emission because they did not have Balmer decrement measurements for their sample. Notwithstanding this *general* agreement, the fraction of objects for which the  $H\alpha$ -based SFR exceeds the UV- (or SED-) based SFR by more than  $1\sigma$  increases from  $f = 0$  to  $f = 0.8$  from  $\text{SFR}(H\alpha) \approx 1$  to  $300 M_{\odot} \text{ yr}^{-1}$ . We formalized this trend by fitting a third-order polynomial to  $\text{SFR}(H\alpha)/\text{SFR}(\text{UV})$  versus  $x \equiv \log[\text{SFR}(H\alpha)/M_{\odot} \text{ yr}^{-1}]$ :

$$\frac{\text{SFR}(H\alpha)}{\text{SFR}(\text{UV})} = 0.29 + 0.31x + 0.29x^2 + 0.0040x^3. \quad (12)$$

Figure 22 shows that  $\gtrsim 40\%$  of galaxies with  $\text{SFR}(H\alpha) \gtrsim 20 M_{\odot} \text{ yr}^{-1}$  have UV- and SED-based SFRs that underpredict the  $H\alpha$ -based SFR by an average factor of  $\approx 2$ . It is unlikely that this trend is due to selection effects because the MOSDEF

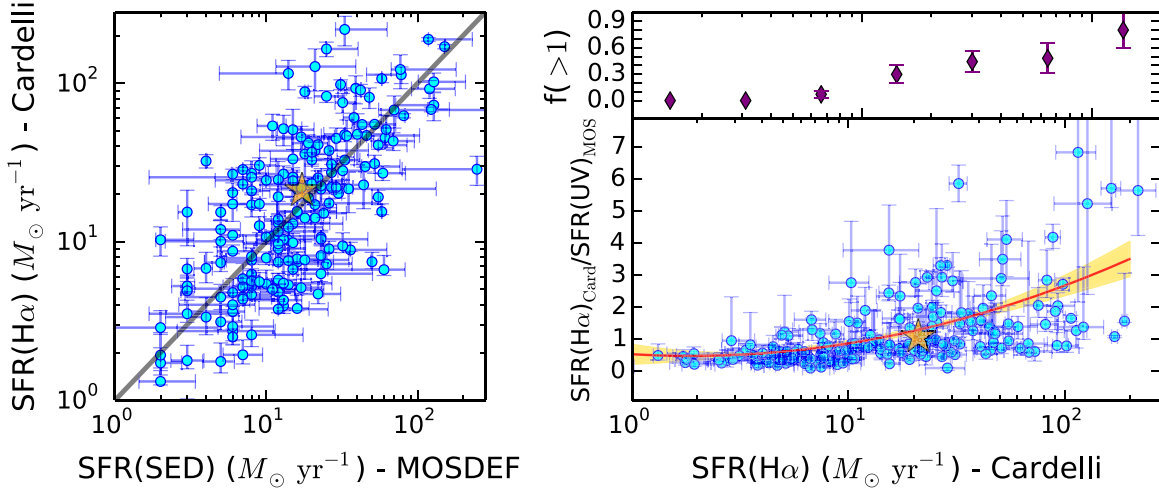


**Figure 22.** Left: comparison of  $\text{SFR}(\text{H}\alpha)$  assuming the Cardelli et al. (1989) extinction curve (and the Balmer decrement), and SED-based SFRs assuming the MOSDEF attenuation curve. Right (bottom): ratio of the dust-corrected  $\text{H}\alpha$  and UV-based SFRs, plotted against  $\text{SFR}(\text{H}\alpha)$ . The UV-based SFR is calculated from the flux of the best-fit SED model at  $1600 \text{ \AA}$ , and corrected for dust assuming  $E(B - V)_{\text{stars}}$ . The red line and shaded region indicate the best-fit third-order polynomial fit and 68% confidence interval between  $\text{SFR}(\text{H}\alpha)/\text{SFR}(\text{UV})$  and  $\log(\text{SFR}(\text{H}\alpha)/M_{\odot} \text{ yr}^{-1})$ . The large stars in both panels denote the average values for the  $\text{H}\beta$ -undetected galaxies. Right (top): fraction of galaxies where  $\text{SFR}(\text{H}\alpha)$  exceeds the UV-based SFR by more than  $1\sigma$ , in bins of  $\text{SFR}(\text{H}\alpha)$ .

galaxy selection is based primarily on rest-optical continuum emission and the success of identifying a redshift depends only on whether any of the rest-optical emission lines are detected, independent of the UV continuum. Thus, it is improbable that we are missing a large number of galaxies where the UV-based SFR is substantially smaller than the  $\text{H}\alpha$ -based SFRs for  $\text{SFR}(\text{H}\alpha) \lesssim 20 M_{\odot} \text{ yr}^{-1}$ .

Focusing on those galaxies with lower SFRs, we find that their  $\text{SFR}(\text{H}\alpha)/\text{SFR}(\text{UV})$  ratios lie systematically below a value of unity. We must address whether this systematic difference is due to variations in the dust attenuation of the nebular regions and stellar continuum, or if there is some other mechanism that may be partly responsible for the low  $\text{SFR}(\text{H}\alpha)/\text{SFR}(\text{UV})$  ratios for these galaxies. To investigate this, we calculated the ratio of the *observed*  $\text{H}\alpha$  and UV SFRs (i.e., uncorrected for dust extinction) for all the objects in our sample (Figure 23). The observed SFRs will include the light emitted by unobscured stars, as well as the unattenuated light from obscured stars. Galaxies with (dust corrected)  $\text{SFR}(\text{H}\alpha) \lesssim 20 M_{\odot} \text{ yr}^{-1}$  have observed  $\text{SFR}(\text{H}\alpha)/\text{SFR}(\text{UV})$  ratios that are generally within  $3\sigma$  of a ratio of unity. As a consequence, for the stars contributing to the observed  $\text{H}\alpha$  and UV luminosities, there is no evidence that we are observing them several tens of Myr after an initial burst of star formation: this scenario would result in observed SFR ratios that deviate from unity due to the different timescales (and mass ranges) over which the  $\text{H}\alpha$  and UV luminosities are sensitive to the total SFR. Thus, if the stars dominating the unobscured  $\text{H}\alpha$  and UV luminosities have a similar IMF and star formation history as those stars that dominate the obscured  $\text{H}\alpha$  and UV luminosities, then the results of Figure 23 suggest that the low dust-corrected  $\text{SFR}(\text{H}\alpha)/\text{SFR}(\text{UV})$  ratios measured for galaxies with  $\text{SFR}(\text{H}\alpha) \lesssim 10 M_{\odot} \text{ yr}^{-1}$  are likely tied to differences in the dust obscuration of the nebular emission and stellar continuum, rather than differences in star formation history, changes in the IMF, or sampling stochasticity (c.f., Lee et al. 2009; Meurer et al. 2009; Fumagalli et al. 2011; da Silva et al. 2014; Domínguez et al. 2014).

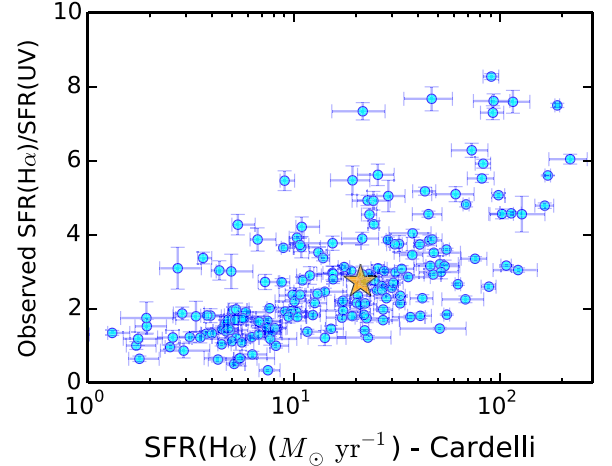


**Figure 23.** Ratio of the observed  $\text{H}\alpha$  and UV SFRs (i.e., uncorrected for dust attenuation) vs. the dust-corrected  $\text{H}\alpha$  SFR. The large star denotes the average values for the  $\text{H}\beta$ -undetected galaxies. Those galaxies with dust-corrected  $\text{SFR}(\text{H}\alpha) \lesssim 10 M_{\odot} \text{ yr}^{-1}$  generally have observed SFR ratios that are consistent with unity within  $3\sigma$ .

#### 4.4.2. A Prescription for Estimating $E(B - V)_{\text{gas}}$ and $A_{\text{H}\alpha}$

With our independent measurements of the color excesses of the stellar continuum and ionized gas, we can quantify the relationship between SED-inferred quantities (i.e.,  $E(B - V)_{\text{stars}}$  and  $\text{SFR}(\text{SED})$ ), which are commonly available for high-redshift galaxy samples, and  $E(B - V)_{\text{gas}}$ , which can be difficult to constrain in the absence of Balmer decrement measurements. Figure 24 shows the difference between gas and continuum color excess ( $E(B - V)_{\text{gas}} - E(B - V)_{\text{stars}}$ ), and the difference between the attenuation of recombination and continuum photons ( $A_{\text{H}\alpha} - A_{\text{cont}}$ ), as a function of the SED-determined sSFR, sSFR(SED). Note that sSFR(SED) combines the SED-determined SFR with the SED-determined stellar mass, so it is not the same as the default sSFR assumed throughout the paper (i.e., the latter combines  $\text{SFR}(\text{H}\alpha)$  with  $M^*$ ). We chose to quantify these relationships in terms of sSFR, and not SFR, because the correlations of

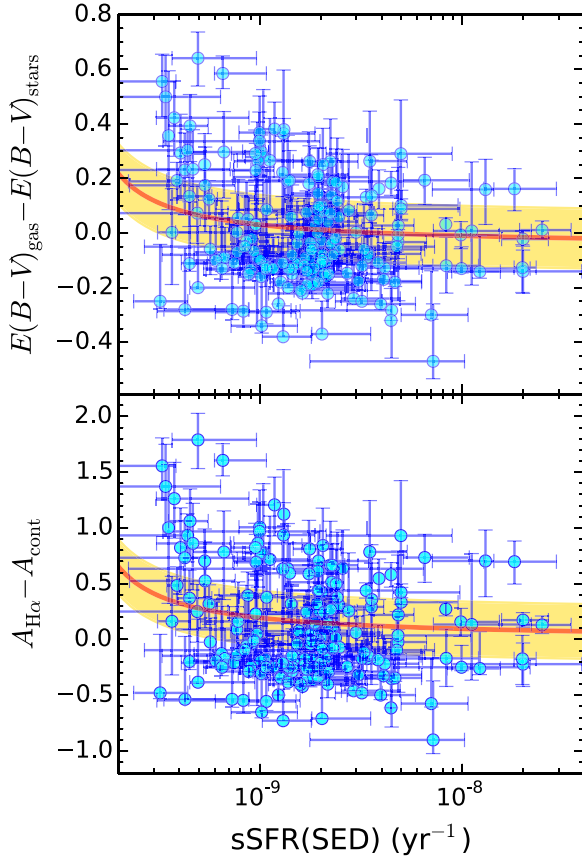


**Figure 24.** Difference between the gas and continuum color excesses (top), and difference between the attenuation (in magnitudes) of the recombination line and continuum photons (bottom) vs.  $s\text{SFR}(\text{SED})$ . Here,  $s\text{SFR}(\text{SED})$  is computed using the SED-based SFR and  $M^*$ . The solid lines and shaded regions denote the best-fit relations and the  $1\sigma$  scatter, respectively, as indicated in the text.

$E(B - V)_{\text{gas}} - E(B - V)_{\text{stars}}$  and  $A_{\text{H}\alpha} - A_{\text{cont}}$  with  $s\text{SFR}(\text{SED})$  are stronger than those with  $\text{SFR}(\text{SED})$ . To establish useful empirical relations between these quantities, we fit them with functions of  $\xi \equiv 1./(\log[s\text{SFR}(\text{SED})/\text{yr}^{-1}] + 10)$ :

$$E(B - V)_{\text{gas}} - E(B - V)_{\text{stars}} = -0.049 + 0.079/\xi, \quad (13)$$

and

$$A_{\text{H}\alpha} - A_{\text{cont}} = -0.0035 + 0.1972/\xi. \quad (14)$$

The scatter in these relations are  $\sigma[E(B - V)_{\text{gas}} - E(B - V)_{\text{stars}}] \approx 0.12$  and  $\sigma[A_{\text{H}\alpha} - A_{\text{cont}}] \approx 0.24$ . Given  $E(B - V)_{\text{stars}}$  and  $s\text{SFR}(\text{SED})$  obtained from standard SED fitting, one can use Equations (13) and (14) to then *roughly* estimate  $E(B - V)_{\text{gas}}$  and  $A_{\text{H}\alpha}$ , keeping in mind the large scatter in these quantities. Finally, note that the difference in color excesses is found to *decrease* on average with increasing  $s\text{SFR}(\text{SED})$  (e.g., see also Price et al. 2014), which is *opposite* the trend that we found between  $E(B - V)_{\text{gas}} - E(B - V)_{\text{stars}}$  and the default  $s\text{SFRs}$  that assume  $\text{H}\alpha$ -based  $\text{SFRs}$  (Figures 16 and 18). This behavior simply reflects the systematic difference between SED-based and  $\text{H}\alpha$ -based  $\text{SFRs}$ , as discussed above.

#### 4.4.3. Summary of SFR Comparisons

The physical picture put forth in the previous section leads to the expectation that UV- (or SED-) based  $\text{SFRs}$  should diverge from  $\text{H}\alpha$ -based ones—which we consider to be more reliable than the former—for galaxies with large  $\text{SFRs}$ , as an increasing fraction of the nebular line and bolometric luminosities arises from regions of a higher dust-covering fraction. The statistics indicating an increasing  $\text{SFR}(\text{H}\alpha)/\text{SFR}(\text{UV})$  ratio with  $\text{SFR}(\text{H}\alpha)$  are consistent with this scheme. A similar effect is seen in the comparison of UV and IR-based  $\text{SFRs}$  (e.g., Goldader et al. 2002; Howell et al. 2010; Reddy et al. 2010), where the former generally underpredict the latter for galaxies where most of the star formation occurs in optically thick regions that are essentially “invisible” in the UV. Because the attenuation curve derived for the continuum is most sensitive to the less-reddened stellar populations in a galaxy, it is not surprising that inferences of total  $\text{SFRs}$  based on the UV continuum emission will underestimate the total  $\text{SFR}$  for very dusty galaxies. The assumption of UV- or SED-based  $\text{SFRs}$  may also lead to erroneous conclusions regarding the dependence of the difference in color excess between the stars and ionized gas, and the  $s\text{SFR}$  (e.g., Figures 16 and 24).

Thus, the common practices of assuming either equal color excesses of the ionized gas and stellar continuum, or assuming that the ionized gas color excess is systematically larger than that of the stellar continuum, may lead to incorrect inferences of the  $\text{SFRs}$ . We also highlight the importance of treating the nebular emission and stellar continuum with the appropriate attenuation/extinction curves. Here, we have made independent measurements of the color excess of the ionized gas (aided by the Balmer decrement), and have calculated the attenuation curve that is relevant for the stellar continuum. Based on these analyses, we find disparities between the  $\text{H}\alpha$ - and UV-based  $\text{SFRs}$  that signify a varying contribution of dusty stellar populations to the bolometric luminosities of high-redshift galaxies.

## 5. CONCLUSIONS

We use a sample of 224 star-forming galaxies at redshifts  $z = 1.36\text{--}2.59$  with measurement of  $\text{H}\alpha$  and  $\text{H}\beta$  emission lines from the MOSDEF survey to investigate the effects of dust on the stellar continuum of high-redshift galaxies. Our analysis suggests that the reddening of the UV continuum with increasing Balmer line opacity is most directly tied to dust obscuration. We calculate the attenuation curve by constructing, and taking ratios of, the composite photometric measurements of galaxies in bins of  $s\text{SFR}$  and Balmer optical depth. The attenuation curve derived here is very similar in shape to that of the SMC curve at  $\lambda \gtrsim 2500 \text{ \AA}$ . Blueward of this wavelength, the curve has a shape that is identical to, but with a normalization that is  $\Delta k(\lambda) \simeq 1.63$  lower than, that of the Calzetti et al. (2000) attenuation curve. Moreover, we find a marginal trend between the depth of absorption at  $2175 \text{ \AA}$  and the color excess of the stellar continuum.

We explore the implications for the attenuation curve on the stellar populations and  $\text{SFRs}$  of high-redshift galaxies. In general, the new attenuation curve implies slightly redder color excesses ( $E(B - V)$ ),  $\approx 20\%$  lower  $\text{SFRs}$ , and stellar masses that are  $\Delta \log(M^*/M_\odot) \approx 0.16$  dex lower than those computed using the typically assumed starburst attenuation curve (Calzetti et al. 2000). We also find that while the color excess

of the ionized gas is similar to that of the stellar continuum for about half of the objects in our sample, the difference in the reddening—and in the total attenuation—of the gas and stars in high-redshift galaxies is a strong function of SFR. In particular, we find that the ionized gas is more reddened relative to the stellar continuum with increasing SFR. Our results are consistent with a simple picture in which the UV through optical continuum of high-redshift galaxies is dominated by a modestly reddened stellar population, while a second, dustier stellar population begins to dominate the bolometric luminosity and nebular line luminosity with increasing SFR. In this picture, UV- and SED-based SFRs may diverge from (i.e., underpredict) the total SFR, even for galaxies with relatively modest  $H\alpha$ -based SFRs ( $\gtrsim 20 M_{\odot} \text{ yr}^{-1}$ ).

Our analysis and results demonstrate the utility of using high-quality near-IR spectroscopic data, along with multi-wavelength photometry, to directly measure the attenuation curve at high redshift. Further spectroscopy from the ongoing MOSDEF survey, along with deep mid- and far-IR imaging data, will allow us to build upon these results, and will be crucial for removing a key uncertainty (namely the shape and normalization of the attenuation curve) in the measurement of star formation rates and the interpretation of stellar populations in the distant universe.

N.A.R. thanks Chuck Steidel, Lee Armus, Daniela Calzetti, and Max Pettini for feedback on the manuscript. We thank the referee for a careful reading of the manuscript and suggestions for clarifying the text. We acknowledge support from NSF AAG grants AST-1312780, 1312547, 1312764, and 1313171. We are grateful to the MOSFIRE instrument team for building this powerful instrument, and to Marc Kassis at the Keck Observatory for his many valuable contributions to the execution of the MOSDEF survey. We also acknowledge the 3D-*HST* collaboration, which provided us with the spectroscopic and photometric catalogs used to select MOSDEF targets and derive stellar population parameters. We also thank I. McLean, K. Kulas, and G. Mace for taking observations for the MOSDEF survey in 2013 May and June. N.A.R. is supported by an Alfred P. Sloan Research Fellowship. M.K. acknowledges support from a Committee Faculty Research Grant and a Hellmann Fellowship. A.L.C. acknowledges funding from NSF CAREER grant AST-1055081. We wish to extend special thanks to those of Hawaiian ancestry on whose sacred mountain we are privileged to be guests. Without their generous hospitality, most of the observations presented herein would not have been possible.

## REFERENCES

- Adelberger, K. L., & Steidel, C. C. 2000, *ApJ*, 544, 218
- Allende Prieto, C., Lambert, D. L., & Asplund, M. 2001, *ApJL*, 556, L63
- Asplund, M., Grevesse, N., Sauval, A. J., Allende Prieto, C., & Kiselman, D. 2004, *A&A*, 417, 751
- Atek, H., Malkan, M., McCarthy, P., et al. 2010, *ApJ*, 723, 104
- Boquien, M., Buat, V., Boselli, A., et al. 2012, *A&A*, 539, A145
- Boquien, M., Calzetti, D., Aalto, S., et al. 2015, *A&A*, 578, 8
- Bouwens, R. J., Illingworth, G. D., Oesch, P. A., et al. 2012, *ApJ*, 754, 83
- Brammer, G. B., van Dokkum, P. G., Franx, M., et al. 2012, *ApJS*, 200, 13
- Bruzual, G., & Charlot, S. 2003, *MNRAS*, 344, 1000
- Buat, V., Giovannoli, E., Heinis, S., et al. 2011, *A&A*, 533, A93
- Buat, V., Marcellac, D., Burgarella, D., et al. 2007, *A&A*, 469, 19
- Buat, V., Noll, S., Burgarella, D., et al. 2012, *A&A*, 545, A141
- Buat, V., Takeuchi, T. T., Burgarella, D., Giovannoli, E., & Murata, K. L. 2009, *A&A*, 507, 693
- Burgarella, D., Buat, V., Takeuchi, T. T., Wada, T., & Pearson, C. 2009, *PASJ*, 61, 177
- Calzetti, D. 2001, *PASP*, 113, 1449
- Calzetti, D., Armus, L., Bohlin, R. C., et al. 2000, *ApJ*, 533, 682
- Calzetti, D., Kinney, A. L., & Storchi-Bergmann, T. 1994, *ApJ*, 429, 582
- Cardelli, J. A., Clayton, G. C., & Mathis, J. S. 1989, *ApJ*, 345, 245
- Chabrier, G. 2003, *PASP*, 115, 763
- Charlot, S., & Fall, S. M. 2000, *ApJ*, 539, 718
- Coil, A. L., Aird, J., Reddy, N., et al. 2015, *ApJ*, 801, 35
- Cowie, L. L., & Barger, A. J. 2008, *ApJ*, 686, 72
- da Silva, R. L., Fumagalli, M., & Krumholz, M. R. 2014, *MNRAS*, 444, 3275
- Daddi, E., Dickinson, M., Morrison, G., et al. 2007, *ApJ*, 670, 156
- Dale, D. A., Cohen, S. A., Johnson, L. C., et al. 2009, *ApJ*, 703, 517
- Domínguez, A., Siana, B., Brooks, A. M., et al. 2014, arXiv:1408.5788
- Domínguez, A., Siana, B., Henry, A. L., et al. 2013, *ApJ*, 763, 145
- Draine, B. T., & Li, A. 2007, *ApJ*, 657, 810
- Dunlop, J. S., McLure, R. J., Robertson, B. E., et al. 2012, *MNRAS*, 420, 901
- Erb, D. K., Steidel, C. C., Shapley, A. E., et al. 2006a, *ApJ*, 647, 128
- Erb, D. K., Steidel, C. C., Shapley, A. E., et al. 2006b, *ApJ*, 646, 107
- Fanelli, M. N., O’Connell, R. W., & Thuan, T. X. 1988, *ApJ*, 334, 665
- Finkelstein, S. L., Papovich, C., Salmon, B., et al. 2012, *ApJ*, 756, 164
- Fitzpatrick, E. L., & Massa, D. 1986, *ApJ*, 307, 286
- Förster Schreiber, N. M., Genzel, R., Bouché, N., et al. 2009, *ApJ*, 706, 1364
- Fumagalli, M., da Silva, R. L., & Krumholz, M. R. 2011, *ApJL*, 741, L26
- Geach, J. E., Smail, I., Best, P. N., et al. 2008, *MNRAS*, 388, 1473
- Goldader, J. D., Meurer, G., Heckman, T. M., et al. 2002, *ApJ*, 568, 651
- Gordon, K. D., Clayton, G. C., Misselt, K. A., Landolt, A. U., & Wolff, M. J. 2003, *ApJ*, 594, 279
- Grogin, N. A., Kocevski, D. D., Faber, S. M., et al. 2011, *ApJS*, 197, 35
- Hopkins, A. M., Connolly, A. J., Haarsma, D. B., & Cram, L. E. 2001, *AJ*, 122, 288
- Howell, J. H., Armus, L., Mazzarella, J. M., et al. 2010, *ApJ*, 715, 572
- Johnson, B. D., Schiminovich, D., Seibert, M., et al. 2007a, *ApJS*, 173, 392
- Johnson, B. D., Schiminovich, D., Seibert, M., et al. 2007b, *ApJS*, 173, 377
- Kashino, D., Silverman, J. D., Rodighiero, G., et al. 2013, *ApJL*, 777, L8
- Kennicutt, R. C. 1998, *ARA&A*, 36, 189
- Kennicutt, R. C., & Evans, N. J. 2012, *ARA&A*, 50, 531
- Kinney, A. L., Bohlin, R. C., Calzetti, D., Panagia, N., & Wyse, R. F. G. 1993, *ApJS*, 86, 5
- Kinney, A. L., Calzetti, D., Bica, E., & Storchi-Bergmann, T. 1994, *ApJ*, 429, 172
- Koekemoer, A. M., Faber, S. M., Ferguson, H. C., et al. 2011, *ApJS*, 197, 36
- Kong, X., Charlot, S., Brinchmann, J., & Fall, S. M. 2004, *MNRAS*, 349, 769
- Kreckel, K., Groves, B., Schinnerer, E., et al. 2013, *ApJ*, 771, 62
- Kriek, M., & Conroy, C. 2013, *ApJL*, 775, L16
- Kriek, M., Shapley, A. E., Reddy, N. A., et al. 2015, *ApJS*, 218, 15
- Kriek, M., van Dokkum, P. G., Franx, M., et al. 2008, *ApJ*, 677, 219
- Lee, J. C., Gil de Paz, A., Tremonti, C., et al. 2009, *ApJ*, 706, 599
- Lee, J. C., Ly, C., Spitler, L., et al. 2012, *PASP*, 124, 782
- Leitherer, C., & Heckman, T. M. 1995, *ApJS*, 96, 9
- Ly, C., Malkan, M. A., Kashikawa, N., et al. 2012, *ApJL*, 747, L16
- Madau, P., & Dickinson, M. 2014, *ARA&A*, 52, 415
- Magdis, G. E., Elbaz, D., Daddi, E., et al. 2010, *ApJ*, 714, 1740
- Mannucci, F., Cresci, G., Maiolino, R., et al. 2009, *MNRAS*, 398, 1915
- Mas-Hesse, J. M., & Kunth, D. 1999, *A&A*, 349, 765
- McLean, I. S., Steidel, C. C., Epps, H. W., et al. 2012, *Proc. SPIE*, 8446, 84460J
- Meurer, G. R., Heckman, T. M., & Calzetti, D. 1999, *ApJ*, 521, 64
- Meurer, G. R., Wong, O. I., Kim, et al. 2009, *ApJ*, 695, 765
- Momcheva, I. G., Lee, J. C., Ly, C., et al. 2013, *AJ*, 145, 47
- Moustakas, J., & Kennicutt, R. C., Jr. 2006, *ApJS*, 164, 81
- Nandra, K., Mushotzky, R. F., Arnaud, K., et al. 2002, *ApJ*, 576, 625
- Noll, S., Pierini, D., Cimatti, A., et al. 2009, *A&A*, 499, 69
- Oesch, P. A., Labbé, I., Bouwens, R. J., et al. 2013, *ApJ*, 772, 136
- Oke, J. B., & Gunn, J. E. 1983, *ApJ*, 266, 713
- Osterbrock, D. E. 1989, *Astrophysics of Gaseous Nebulae and Active Galactic Nuclei* (Mill Valley, CA: University Science Books)
- Overzier, R. A., Heckman, T. M., Wang, J., et al. 2011, *ApJL*, 726, L7
- Pannella, M., Carilli, C. L., Daddi, E., et al. 2009, *ApJL*, 698, L116
- Papovich, C., Rudnick, G., Rigby, J. R., et al. 2009, *ApJ*, 704, 1506
- Pei, Y. C. 1992, *ApJ*, 395, 130
- Pettini, M., & Pagel, B. E. J. 2004, *MNRAS*, 348, L59
- Prevot, M. L., Lequeux, J., Prevot, L., Maurice, E., & Rocca-Volmerange, B. 1984, *A&A*, 132, 389
- Price, S. H., Kriek, M., Brammer, G. B., et al. 2014, *ApJ*, 788, 86

- Reddy, N., Dickinson, M., Elbaz, D., et al. 2012a, *ApJ*, 744, 154
- Reddy, N. A., Erb, D. K., Pettini, M., Steidel, C. C., & Shapley, A. E. 2010, *ApJ*, 712, 1070
- Reddy, N. A., Pettini, M., Steidel, C. C., et al. 2012b, *ApJ*, 754, 25
- Reddy, N. A., & Steidel, C. C. 2004, *ApJL*, 603, L13
- Reddy, N. A., & Steidel, C. C. 2009, *ApJ*, 692, 778
- Reddy, N. A., Steidel, C. C., Fadda, D., et al. 2006, *ApJ*, 644, 792
- Reddy, N. A., Steidel, C. C., Pettini, M., et al. 2008, *ApJS*, 175, 48
- Sanders, R. L., Shapley, A. E., Kriek, M., et al. 2015, *ApJ*, 799, 138
- Scoville, N., Faisst, A., Capak, P., et al. 2015, *ApJ*, 800, 108
- Seibert, M., Martin, D. C., Heckman, T. M., et al. 2005, *ApJL*, 619, L55
- Shim, H., Chary, R.-R., Dickinson, M., et al. 2011, *ApJ*, 738, 69
- Shivaei, I., Reddy, N. A., Steidel, C. C., & Shapley, A. E. 2015, *ApJ*, 804, 149
- Siana, B., Smail, I., Swinbank, A. M., et al. 2009, *ApJ*, 698, 1273
- Siana, B., Teplitz, H. I., Chary, R.-R., Colbert, J., & Frayer, D. T. 2008, *ApJ*, 689, 59
- Silverman, J. D., Green, P. J., Barkhouse, W. A., et al. 2008, *ApJ*, 679, 118
- Skelton, R. E., Whitaker, K. E., Momcheva, I. G., et al. 2014, *ApJS*, 214, 24
- Sklias, P., Zamojski, M., Schaerer, D., et al. 2014, *A&A*, 561, A149
- Sobral, D., Best, P. N., Matsuda, Y., et al. 2012, *MNRAS*, 420, 1926
- Stecher, T. P., & Donn, B. 1965, *ApJ*, 142, 1681
- Steidel, C. C., Rudie, G. C., Strom, A. L., et al. 2014, *ApJ*, 795, 165
- Wang, B., & Heckman, T. M. 1996, *ApJ*, 457, 645
- Wild, V., Charlot, S., Brinchmann, J., et al. 2011, *MNRAS*, 417, 1760
- Wilkins, S. M., Bunker, A., Coulton, W., et al. 2013, *MNRAS*, 430, 2885
- Wuyts, S., Förster Schreiber, N. M., Lutz, D., et al. 2011, *ApJ*, 738, 106
- Wuyts, S., Förster Schreiber, N. M., Nelson, E. J., et al. 2013, *ApJ*, 779, 135
- Yoshikawa, T., Akiyama, M., Kajisawa, M., et al. 2010, *ApJ*, 718, 112